Planetary Boundary Layer Turbulence

In previous chapters boundary layers were evident as thin layers across which thermal, dynamic, and material properties of a free interior flow make a transition to their boundary values and/or boundary fluxes. In those cases the thinness of the boundary layer was typically a statement of the smallness of the relevant diffusivity; *e.g.,* the depth h of the laminar Ekman boundary layer scales as $\nu^{1/2}$ (*Shear Turbulence*) and the thermal boundary layer in convection scales as either $\kappa^{2/3}$ or $\kappa^{4/7}$ in soft or hard turbulence regimes (*Convective Turbulence*). Boundary layers are also evident in geophysical flows, for instance at the bottom of the atmosphere, and at the top and bottom of the ocean. And, they serve essentially the same purpose: to match a free or interior flow to the conditions imposed at the surface, *i.e.,* no-slip, fixed temperature, specified material properties, or specified boundary fluxes.

Unlike boundary layers in many engineering flows, these planetary boundary layers (or PBLs) are almost always turbulent. The turbulence expresses the instability of the laminar boundary layer solutions, thus giving rise to an effective (eddy) diffusivity that allows the flow to make the transition between its surface and free-flow properties over a much deeper layer than would occur with only molecular diffusion and no turbulent mixing. Through this layer turbulent vertical fluxes, $\overline{w'\mathbf{u}'_h}$ and $\overline{w'c'}$, are expected to be significant in shaping the mean vertical profiles, $\overline{\mathbf{u}}_h(z)$ and $\overline{c}(z)$, where c is any material property. To have any asymptotic utility, the concept of a PBL also requires that its depth h remain much smaller than the vertical scale of the free flow. The PBL in the ocean and atmosphere is typically tens or hundreds of meters thick, respectively; this is thin compared to the 3-10 km depth scale of free oceanic and atmospheric flows. Some authors prefer to define the PBL as that layer of the atmosphere that intensively, or actively, mediates the exchanges with the underlying surface (in the case of the atmosphere) or the overlying atmosphere (in the case of the ocean), but such a characterization fails to ensure the thinness of the layer that is fundamental to its identification as a special layer.

The basic mechanisms for generating turbulence with in the PBL are familiar: shear and buoyancy. However these usual suspects take on unusual guises in many geophysical situations. Consider the following:

- Shear boundary layers are usually influenced by Earth's rotation, at least on time scales longer than several hours (*i.e.,* Ekman layers). This limits the otherwise unbounded growth in the layer thickness seen in non-rotating shear layers , unless stable stratification further limits the thickness.

- For PBLs in the upper ocean, solar radiation may be absorbed over a depth of order h and may act to stabilize flows that are otherwise destabilized by a boundary shear stress.

- Both the atmosphere and ocean are two component fluids, whose minor constituents (moisture and salinity), contribute significantly to density fluctuations. In the case of the atmosphere, the degree that moisture and thermal fluctuations project onto density (buoyancy) depends strongly on whether or not the fluid is saturated.

- In the atmosphere, moisture, and particularly condensed moisture, strongly modulates the emission, absorption, and reflection of radiant streams of energy, and this in turn helps determine the rate that radiative processes stabilize or destabilize the flow.

- Infrared emission and absorption confined to thin boundaries — for instance at the top of the PBL in the upper ocean, or along the interior edge of stratocumulus topped boundary layers — can significantly affect the buoyancy forcing of turbulence.
- Surface gravity waves provide a different type of boundary than land and sea-bottom topography because they are a moving surface. The gravity wave effects are somewhat different in the air and water marine PBLs. The turbulence above a spatially and temporally varying boundary is quite different than above a flat boundary, whether smooth or rough.
- In upper ocean PBLs, wave breaking may be an important source of turbulence, while terrain effects and wave breaking may contribute strongly to turbulent transports in stably stratified atmospheric PBLs.

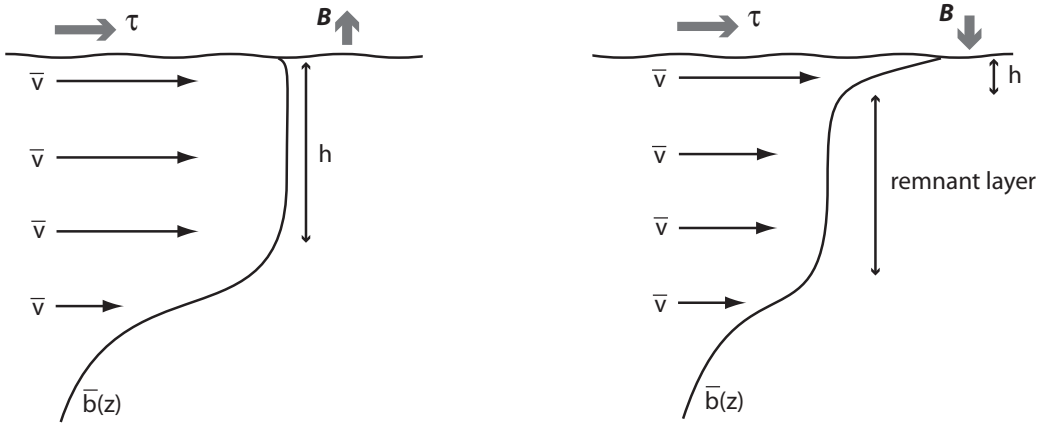

Figure 1: Schematic showing an oceanic mixed layer at night with net infrared and evaporative surface cooling (left) and a shallower daytime oceanic PBL with solar heating above a remnant layer (right).

Geophysical boundary layers go through cycles — diurnally, synoptically, and seasonally. Since the sign of $\mathcal{B}$ strongly influences the PBL depth h, we often see vertical profiles like the two classes sketched in Fig. 1. Under convective forcing, the boundary layer tends to be deeper and its mean profiles more nearly well-mixed. Under stable forcing, the layers are shallower, the profiles have bigger gradients, and often the residual (or remnant)[1] decaying turbulence of a previously deeper PBL layer is evident beyond the currently active one. Convective forcing and/or deep layers are more prevalent in the oceanic winter (high winds and weak insolation), oceanic night (infrared radiative cooling and evaporation), atmospheric storms (high winds), and atmospheric day (surface heating by insolation). Stable forcing and/or shallow layers are more prevalent in the oceanic summer and daytime (solar absorption), in the atmospheric night (infrared radiative cooling), and during weak winds. There are also significant climatological gradients in the PBL depth (*e.g.,* deep convective layers in the atmospheric tropics and oceanic sub-polar zones), as well as synoptic and mesoscale gradients related to their larger eddy flow patterns.

[1]The atmospheric literature prefers the former terminology, while the oceanic literature prefers the latter.

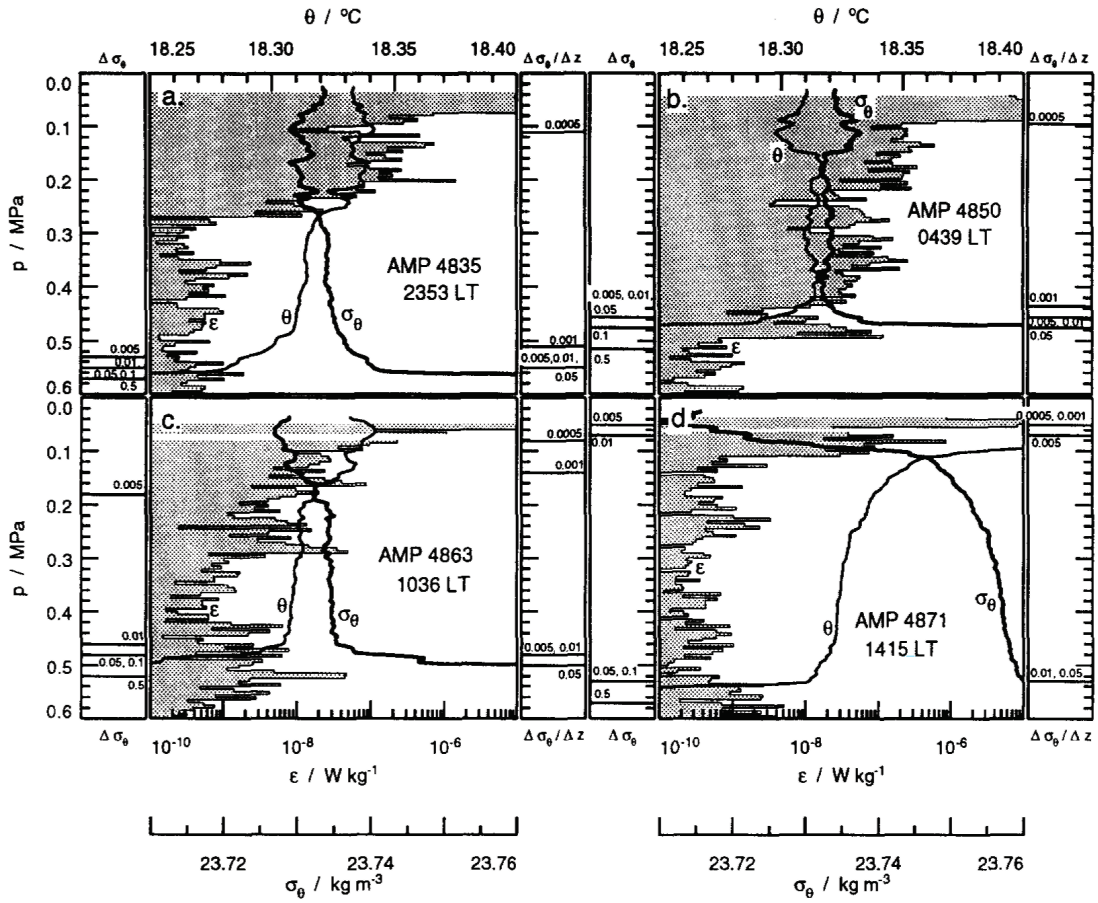

Figure 2: Profiles of dissipation rate ε, θ and σ_θ taken at four stages of the diel cycle. Clockwise from upper left: (a) convective deepening phase; (b) convective equilibrium in a deep mixed layer extending to seasonal thermocline; (c) developing diurnal thermocline; (d) strong diurnal thermocline. At left are the estimates of mixed layer depth based on density difference criteria, and at the right are mixed layer depths based on density gradient criteria. The "depth" scale here is pressure, which is mostly hydrostatic with 1 MPa $\approx$ 100 m. (Brainerd and Gregg, 1995)

An illustration of a diel (daily) cycle in the upper ocean is shown in Fig. 2, for both $\overline{b}(z,t)$ and $\epsilon(z,t)$, from microstructure measurements with a slowly dropping instrument. Here the PBL depth varies from about 10-50 m, and the dissipation rate varies by several orders of magnitude. The ways that the diel cycle is manifest on the atmospheric winds at two levels is shown in Fig. 3. During the night, when buoyancy stabilizes the flow, the winds at 50 and 0.5 m are strongly differentiated. While during the day, when heating at the surface forces convective eddies that mix a deep layer, the winds are well mixed through 50 m.

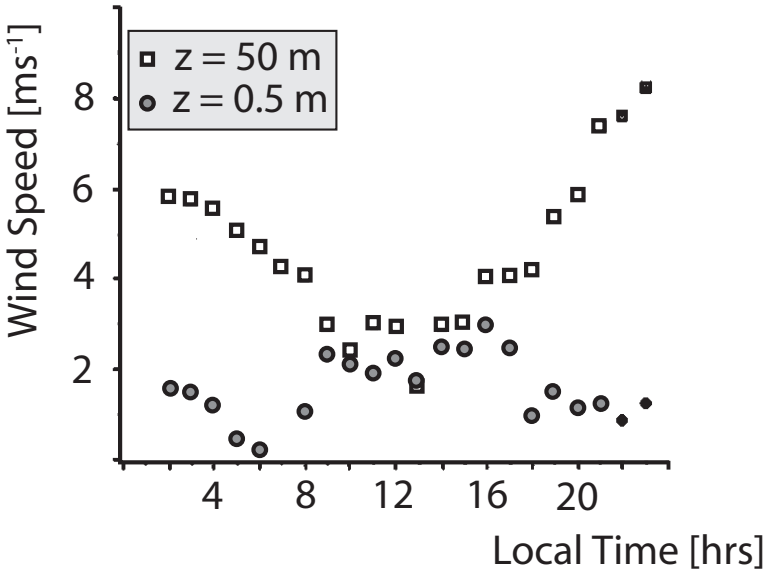

Figure 3: Daily march of winds at two levels as observed during day 33 of the Wangara, Australia experiment (Sorbjan, 1989)

The daily cycling of the PBL over land — from a shallow, stably-stratified state at night to a deep, well-mixed state during the daytime hours — means that in the morning hours the PBL can be expected to grow through the remnants of the previous day's mixed layer. Because the stratification is so weak, this growth can be explosive, at least until the height of the previous day's mixed layer is reached. Thereafter subsequent deepening is slowed by the stratification within the free-troposphere. This tendency of the previous layer to be left as a residual layer above the night time boundary layer can be important to atmospheric chemistry; it separates the previous days pollutants from emissions at the surface during the night. These are mixed when the boundary layer re-forms in the morning, and this can be a time of very interesting chemistry. On longer timescales it also can bias estimates of material transport. For example, photosynthesis by plants during the day draws down CO_2 from the reservoir of a relatively deep, dilute PBL, while its counterpart, respiration by microbes in the soil, tends to dominate at night when the PBL is stably stratified and shallow. Such effects, when not properly accounted for, produce biases in estimates of carbon uptake derived from near-surface measurements of CO_2 in the atmosphere. Because the seasonal cycle of boundary layer depth correlates with cycles of photosynthesis and respiration, similar biases are also evident on seasonal timescales. Hence an understanding of boundary layer processes is critical to the quantification of material budgets.

1 Surface Layer

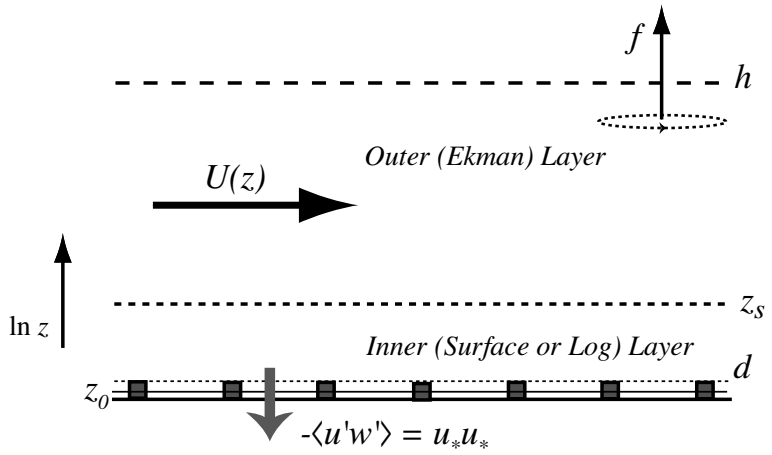

Figure 4: Schematic of inner and outer layers within the shear PBL.

Although we speak of the PBL as a single layer, it typically is comprised of several layers, as illustrated in Fig. 4 for the case of a neutrally stratified shear layer. Viscous forces and the details of the surface may be important on the scale d for the individual roughness elements (centimeters to tens of meters) that defines the *roughness sub-layer*, while the large eddies, whose scale is commensurate with the boundary layer depth $h \gg d$, dominate the turbulent transport through the bulk of the boundary layer. If h and d are sufficiently well separated, there may be a range of intermediate scales near, but not immediately abutting, the boundary $h \gg z \gg d$, for which one can make a similarity hypothesis that z is the only relevant length-scale. Doing so defines the surface layer. The concept of a surface layer is fundamental to boundary layer turbulence, because it sweeps all of the details of the surface shape under the rug through the definition of a virtual boundary height z_0 that characterizes the surface roughness. The existence of a surface layer encourages the nomenclature of the inner and outer layers regions of the PBL as a whole (Fig. 4).

In a neutrally stratified fluid, the surface-layer scaling is just that given in *Shear Turbulence*,[2] *i.e.,* the *law of the wall*:

$$u(z) = k^{-1} u_* \ln(z/z_0)\,, \tag{1}$$

where u_* is the friction velocity (*i.e.,* the square root of the surface stress divided by density) and $k = 0.4$ is von Karman's constant. z_0 is the roughness length and is defined as the height above the surface where the extrapolated velocity profile (1) vanishes. Although z_0 is determined empirically by this extrapolation procedure, for simple rough surfaces (grains of sand) it can be shown to be a function of the height and spatial density (*i.e.,* closely packed versus sparse) of the roughness elements. Typical values for empirically determined z_0 are listed in Table 1. Note that the values are typically much smaller than the size d of the actual roughness elements (*e.g.,* a tree in a forest).

[2]This can be derived most simply as a scaling theory, but it also can be derived more formally as a matched asymptotic expansion in an overlap region between a smooth-boundary viscous sublayer and an inertial interior layer; see the *Shear Turbulence* lecture notes.

surface	z_0 [m]
water	0.0001 - 0.001
bare soil	0.001 - 0.01
crops	0.005 - 0.05
forest	0.5

Table 1: Approximate roughness heights for various surfaces.

In geophysical flows, rotation might be expected to play a role in the nature of the near surface matching. The fact that it does not (insofar as the law of the wall is valid) is often expressed in terms of what is called Rossby number similarity, where the surface Rossby number $Ro = u_*/(fz_0)$ (a measure of the ratio of the local vorticity on the scale of roughness elements to the planetary vorticity) is large. Although planetary rotation can generally be neglected in the surface layer, buoyancy cannot. To incorporate buoyancy into the surface-layer scaling, Obukhov postulated that the non-dimensional shear should be a function of the non-dimensional height,

$$\zeta = z/L, \qquad \text{where} \qquad L = -\frac{u_*^3}{k\mathcal{B}}. \tag{2}$$

The length-scale L chosen to non-dimensionalize z measures the height where the local production of turbulence by the shear-stress exactly balances the rate of working against (assuming $\mathcal{B} < 0$) the mean state stability. It is called the Obukhov length (sometimes Monin-Obukhov). Hence ζ measures the relative importance of shear and buoyancy to the development of turbulence kinetic energy. The shear-flow limit corresponds to $L = \pm\infty$ or $\zeta = 0$ (but not $z = 0$ where the surface-layer formula is not valid). Convective flows have upward buoyancy flux, $\mathcal{B} > 0$, hence $\zeta < 0$. Stable shear boundary layers have $\mathcal{B} < 0$ and $\zeta > 0$; sometimes a distinction is made between weakly and strongly stable surface layers based on whether ζ is greater than or less than one.

1.1 Monin-Obukhov Similarity Theory

The generalization of the *law of the wall* to account for buoyancy and shear is referred to as Monin-Obukhov (or simply M-O) similarity theory. It postulates that

$$\left(\frac{kz}{u_*}\right)\frac{d\overline{u}}{dz} \;=\; \Phi_m(\zeta)\,. \tag{3}$$

Here Φ_m is the non-dimensional shear, also called the non-dimensional flux profile, the flux-gradient relation, or the stability function. To reproduce the law of the wall Φ_m should approach unity as $\zeta \to 0$. Since we expect that the flow will be less stratified when buoyancy contributes to mixing, and more stratified when buoyancy resists mixing, then we might expect that $\Phi_m > 1$ for $\zeta > 0$ and $\Phi_m \leq 1$ otherwise. Analogously,

$$\left(\frac{kz}{T_*}\right)\frac{d\overline{T}}{dz} = \Phi_h(\zeta), \tag{4}$$

$$\left(\frac{kz}{c_*}\right)\frac{d\overline{c}}{dz} = \Phi_h(\zeta), \tag{5}$$

where T is temperature and c is some material property (*e.g.,* salinity, or specific humidity). (For atmospheric flows, it is more appropriate to use θ than T to eliminate compressional heating.) T_* and c_* are flux scales defined in analogy to u_* such that:

$$u_* T_* = -\overline{w'T'} \quad \text{and} \quad u_* c_* = -\overline{w'c'}\,. \tag{6}$$

The fact that Φ_h appears in both (4) and (5) reflects the assumption that the non-dimensional material gradient function is independent of the particular material property being scaled (this need not be true).

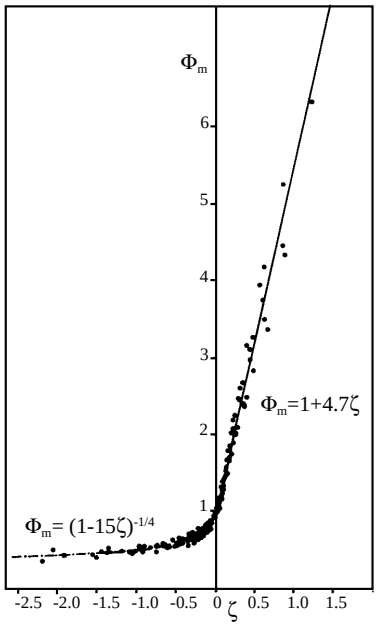

Figure 5: Non-dimensional shear function for the Monin-Obukhov similarity model (also called the stability function). (Adapted from Businger, 1970, Fig. 2.1)

Many experiments have been conducted to experimentally evaluate the theory, and within the range of expected validity the theory can be considered to be a great success. That is, the non-dimensional gradient functions do indeed exhibit universality given the assumptions of the theory (*i.e.,* $h \gg z \gg d$, $Ro \gg 1$, steady flow, *etc.*). An illustration of the ability of this non-dimensionalization to collapse the data is given in Fig. 5, where Φ_m is derived from a series of measurements made over wheat stubble in Kansas. Many similar measurements have been made over a wide variety of surfaces with the result being that

$$\Phi_m \approx \begin{cases} 1 + \beta_m \zeta & \zeta > 0 \\ (1 - \gamma_m \zeta)^{a_m} & \zeta \leq 0 \end{cases} \tag{7}$$

$$\Phi_h \approx \begin{cases} 1 + \beta_h \zeta & \zeta > 0 \\ (1 - \gamma_h \zeta)^{a_h} & \zeta \leq 0 \end{cases}. \tag{8}$$

For our purposes it is sufficient to take $\beta_h = \beta_m = 5$, $\gamma_h = \gamma_m = 16$, $a_m = -1/4$ and $a_h = -1/2$. The actual values of these constants is a matter of some debate with most studies finding that

$5 < \beta_m < 7$, $5 < \beta_h < 9$, $16 < \gamma_m < 20$, and $12 < \gamma_h < 16$. These fits are accurate for $|\zeta|$ values that are not too large, but for $|\zeta| \gg 1$, little reliable data exists. Instead the general shape of the gradient functions is constrained by asymptotic considerations that, as we shall see below, argues for different values of a_m and a_h than those given above.

The general form of (7) and (8) allows one to analytically integrate (3)-(5), thereby yielding non-dimensional profile functions:

$$u(z) = \frac{u_*}{k} \left[\ln(z/z_0) - \Psi_m(\zeta) + \Psi_m(z_o/L) \right] \tag{9}$$

$$T(z) - T(z_0) = T_* \left[\ln(z/z_0) - \Psi_h(\zeta) + \Psi_h(z_0/L) \right] \tag{10}$$

where for $\zeta \geq 0$

$$\Psi_m = -\beta_m \zeta \quad \text{and} \quad \Psi_h = -\beta_h \zeta \, . \tag{11}$$

While for $\zeta < 0$

$$\Psi_m = 2 \ln \left(\frac{1 + \Phi_m^{-1}}{2} \right) + \ln \left(\frac{1 + \Phi_m^{-2}}{2} \right) - 2 \tan^{-1}(\Phi_m^{-1}) + \frac{\pi}{2} \tag{12}$$

$$\Psi_h = 2 \ln \left(\frac{1 + \Phi_h^{-1}}{2} \right) \, . \tag{13}$$

We should note that $T(z_0)$ is not necessarily the surface temperature, but for simple surfaces it should be close to this value, and so we will subsequently take it as such. Actually estimating the flux, given $T(z)$ and $u(z)$, requires us to solve the equations above for u_* and T_*. Because L depends on u_* and T_*, this is not as trivial a procedure as we might hope, nonetheless the dependencies are simple enough in the stable case to yield closed form expressions. In the unstable case we must resort to iteratively solving a system of implicit equations for the flux.

It is difficult to overstate the importance of these results. They provide a means for estimating the flux from the profiles and are used in some form in virtually every atmospheric or oceanic flow solver that requires some surface boundary conditions. They are undoubtedly the most important result from similarity theory in atmospheric and oceanic sciences.

1.2 Monin-Obukhov Extensions

Eddy Viscosity and Dissipation: Accompanying the mean profiles are other log-layer properties: (1) the eddy momentum flux is in the direction of the mean surface stress $\hat{\mathbf{e}}_\tau$ and is constant with height in the surface layer,

$$\overline{\mathbf{u}' w'}(z) = - \hat{\mathbf{e}}_\tau u*^2 \, ; \tag{14}$$

(2) the eddy viscosity varies linearly with height,

$$\nu_e(z) = - \frac{\overline{u' w'}}{\partial_z \overline{u}} = k u_* z \, ; \tag{15}$$

and (3) the kinetic energy dissipation varies inversely with height,

$$\varepsilon(z) = \nu_e(z) (\partial_z \overline{u})^2 = \frac{u_*^3}{kz} \, , \tag{16}$$

where obviously the final relation cannot be taken all the way to $z = 0$. With MO similarity, there are stability-function generalizations of these relations.

Mixing-Length Theory: The non-dimensional gradients implicitly embody the mixing-length hypothesis. For

$$K_m = -\overline{u'w'}\left(\frac{d\overline{u}}{dz}\right)^{-1} \tag{17}$$

and similarly for K_h, MO theory requires that

$$K_m = kzu_*\Phi_m^{-1} \tag{18}$$

$$K_h = kzu_*\Phi_h^{-1}\ . \tag{19}$$

These indicate that in a mixing length theory of turbulent flows K_m and K_h should depend on the stability following the stability dependence of Φ_h and Φ_m. From the result in previous chapters, we do not expect turbulence for Ri values greater than about 1/4. Thus we expect the empirically derived values of Φ_m and Φ_h to become infinite as the stable stratification increases, L decreases, and ζ increases, and indeed they do. Equations (18) and (19) also provide a basis for deriving a turbulent Prandtl number

$$Pr_e = \frac{K_m}{K_h} = \frac{\Phi_h}{\Phi_m}\ . \tag{20}$$

Thus we see, for stable through neutral coefficients, (7) and (8) imply a Pr_e value one. As the flow becomes increasingly convective, Pr_e decreases, indicating rather more efficient turbulent transport of heat relative to momentum, as could be expected from the transport efficiency of buoyant plumes.

Higher-Order Moments: The similarity hypothesis does not need to be restricted to a scaling of the mean gradients. It can be extended to non-dimensionalize second- and higher-order moments. The same experiments that demonstrated the universality of Φ_m and Φ_h also demonstrate that the second order quantities, when appropriately non-dimensionalized, are also universal. So that

$$\frac{\overline{u_i'u_j'}}{u_*^2} = \Phi_{ij}(\zeta), \quad \frac{\overline{u'T'}}{u_*T_*} = \Phi_{1\theta}(\zeta), \quad \frac{\overline{T'T'}}{T_*T_*} = \Phi_{\theta\theta}(\zeta), \quad \text{and} \quad \frac{\theta_\varepsilon z}{u_*^3} = \Phi_\varepsilon(\zeta)\ . \tag{21}$$

Free Convection: A special limit of the MO theory is free convection, wherein $\zeta \to -\infty$. In this limit it has been proposed that the surface stress (effectively u_*) ceases to be a parameter, hence the list of parameters produces no non-dimensional parameters, and similarity implies that non-dimensional profiles must be universal. Here, following Wyngaard *et al.* (1971), the available parameters allow us to define the local convective velocity and temperature scales,

$$w_f = (\mathcal{B}z)^{1/3} \tag{22}$$

$$T_f = (g/\theta_0)^{-1}\frac{\mathcal{B}}{w_f} \tag{23}$$

that are used as the basis for arguing that

$$\frac{kz}{T_f}\frac{dT}{dz} = \text{const.}\ . \tag{24}$$

Equation (24) implies that the temperature profile near the surface should scale as $z^{-1/3}$. Multiplying both sides of (24) by u_*/w_f suggests that

$$\lim_{\zeta \to -\infty} \Phi_h \propto -\zeta^{-1/3} \, . \tag{25}$$

We note that this limit is not respected by the empirical fit given in (7). The differences in exponents are, however, not large (-1/2 versus -1/3), and it may well be that the data underlying (7) is insufficient to constrain the asymptotic behavior of the fit. Attempts to correct for this and constrain the shape of Φ_m and Φ_h based on asymptotic corrections have led to a wide variety of proposals for their basic form, most of which are very similar in regions well constrained by data (*i.e.,* occur commonly in nature).

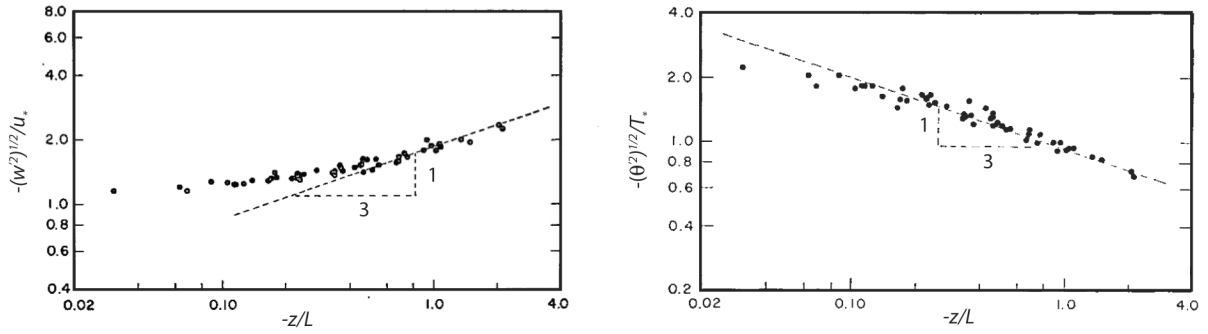

Figure 6: $\Phi_{33}^{1/2}$ and $\Phi_{\theta\theta}^{1/2}$ based on data from the Kansas field program of the AFCRL. (Wyngaard *et al.*, 1971)

Free convective scaling can also be used as a basis for arguing that

$$\frac{\overline{w'w'}}{w_f^2} = \text{const.} \, , \tag{26}$$

hence that

$$\lim_{\zeta \to -\infty} \Phi_{33} \propto -\zeta^{2/3} \, . \tag{27}$$

This is the variance of vertical velocity that can be expected to increase with $z^{2/3}$ in the surface layer (*i.e.,* for z values much less than the depth of the PBL). Empirical support for this scaling relation, and a similar scaling applied to $\Phi_{\theta\theta}$, is shown in Fig. 6. Similar arguments would also suggest that $\Phi_{11} \propto \Phi_{22} \propto z^{2/3}$, which is not supported by the data. In the case of the non-dimensional variances of horizontal velocity, it appears that other factors are important, most likely the large-eddies whose splatting at the surface induces outer-scale fluctuations in the variances of u and v that might be expected to scale with the PBL depth h (not accounted for in the above arguments).

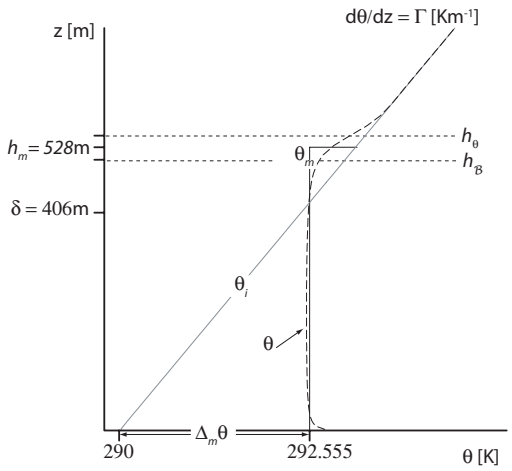

Figure 7: Development of a convective boundary layer under the action of a constant surface heat flux Q_0. Shown are the initial profile θ_i (light diagonal line); the profile calculated using LES at $t = 48000$s (dashed line); and equivalent mixed layer constructed as discussed in text, θ_m (dark solid line). Also shown are the four heights, $\delta,\ h_{\mathcal{B}},\ h_m$ and h_θ.

2 Convective Boundary Layers

2.1 Dry Boundary Layers

The prototype problem for dry convective boundary layers (CBLs) is a thermal layer growing into a uniformly stratified (*i.e.,* constant Γ) fluid under the action of a constant surface heat flux Q_0 (Fig. 7). The initial temperature profile is specified as

$$\theta_i \equiv \theta(z, t = 0) = \theta_0 + \Gamma z \ . \tag{28}$$

For $Q_0 > 0$, we expects a deepening thermal boundary layer. Empirically such developing layers exhibit several characteristics across an effectively three-layer structure. Near the ground, for $z/h \ll 1$, a surface layer is apparent where the profiles should obey the free convective scaling. Above this, and through the bulk of the layer, material properties are generally well-mixed, hence this layer is often referred to as the *mixed layer*. At the top of the layer, at $z/h \approx 1$, a region of enhanced stability is apparent that matches the non-stratified interior to the stratified free-flow. All of these features are evident in Fig. 7, and each of them arises spontaneously from the development of the turbulent flow.

δ is defined as the encroachment depth, *i.e.,* the depth of penetration of a well-mixed layer connected to the surface whose heat content change from the initial stratified profile is exactly equal to the time integral of the heat loss associated with the surface flux. One might naively think that δ is the boundary layer depth, but this is not correct because there is additional turbulent mixing into the stratified layer above the well-mixed layer, referred to as entrainment. To describe the evolution of the depth of the thermal layer depth h, it is useful to interpret the flow in terms of

an equivalent mixed layer depth h_m that we define as

$$h_m = \frac{\Delta_m\theta}{\Gamma}\left(1+\sqrt{1+\frac{2Q_0\Gamma t}{(\Delta_m\theta)^2}}\right) , \tag{29}$$

where

$$\Delta_m\theta \equiv \left(2\Gamma\int_0^\infty (\theta-\theta_i)\,H(\theta-\theta_i)\,\mathrm{d}z\right)^{1/2} , \tag{30}$$

with $H(x)$ the Heaviside function. $\Delta_m\theta$ measures the entropy increase of the component of the boundary layer that has warmed compared to the initial state. Hence h_m measures the depth of a mixed layer whose region of warming has the same mean potential temperature as the actual layer of interest. To make this definition energetically consistent, θ should be replaced by θ_v when working with moist layers, while for freely convecting oceanic layers a description simply in terms of T will suffice. Note that the definition of $\Delta_m\theta$ above defines the potential temperature of this mixed layer as $\theta_m = \theta_0 + \Delta_m\theta$,; this also being illustrated in Fig. 7.

The equivalent mixed-layer depth h_m differs from more familiar measures of the PBL depth, such as h_θ, which associates the boundary layer depth with the height where $\partial_z\theta$ is a maximum, or what we call $h_\mathcal{B}$, the height where the buoyancy flux profile, $\mathcal{B}(z)$, is a minimum. However, because h_m is based on an integral measure of the PBL heat content, it tends to provide a more robust estimate of the PBL depth than either h_θ or $h_\mathcal{B}$, both of which depend on the structure of a profile at a point. Both h_θ and $h_\mathcal{B}$ may be more suitable for empirical studies, where the initial state temperature profile may be ill-defined, but they tend to be ill-defined for the mixed-layer idealization of the PBL thickness that motivates the introduction of h_m. For comparison, one can imagine a well-mixed boundary layer that is nowhere gravitationally unstable and extends no farther into the stratified interior region than is required by the growing heat content imposed by the positive surface heat flux Q_0. This is sometimes called encroachment or non-penetrative convection, with

$$\theta(z,t)\geq\theta_i(z) \quad \forall\{z,t\} \quad\Longrightarrow\quad (\Delta_m\theta)^2 = 2\Gamma Q_0 t \quad \text{hence} \quad h=\delta\equiv\left(\frac{2Q_0t}{\Gamma}\right)^{1/2} . \tag{31}$$

so h is well defined and is equal to the encroachment depth δ. To the extent the actual boundary layer profile approaches a well-mixed shape, these various measures of h converge to the same value, although in reality departures from well-mixed tend to result in $\delta < h_\mathcal{B} < h_m < h_\theta$. The statement that δ is smaller than the other depth measures is equivalent to the statement that some fluid from the stably stratified region aloft is being drawn into the actively turbulent boundary layer, *i.e., entrainment* of warm interior air is occurring (Fig. 8).

For small diffusivities, large temperature gradients can be expected to develop that for sufficiently small viscosity will lead to the development of convective eddies and turbulent circulations within the boundary layer. These eddies are responsible for the homogenization of the flow through the depth of the boundary layer and initiate additional mixing (entrainment) between the free-troposphere and the surface. An example of such processes is illustrated in Fig. 8; it shows the spatial structure and temporal evolution in the vicinity of a convective plume impinging on the region of stable stratification topping the mixed layer. The overshooting of the eddy flow results in the region of enhanced stratification near the top of the PBL and is accompanied by the engulfment

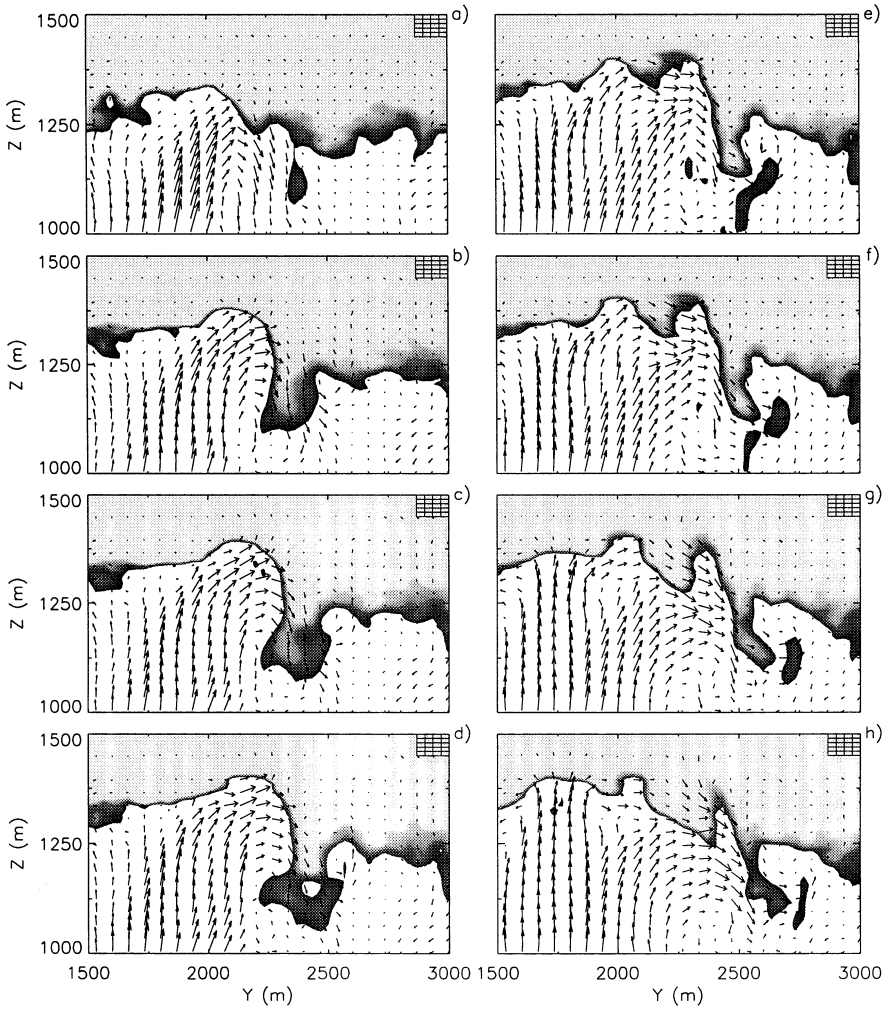

Figure 8: Temporal and spatial evolution of the entrainment interface in a sub-domain of a convective boundary layer as represented by large-eddy simulation. Temperature is contoured, and flow vectors are shown by arrows. For clarity only every third vertical, and every second horizontal grid point is shown. Panels (b)-(h) are 107, 134, 161, 228, 255, 295, and 335 s, respectively, later than (a). (Sullivan *et al.*, 1998)

of free tropospheric air at its edges. This expresses the entrainment process, at least for situations where convective eddies are sufficiently strong relative to the overlying stratification to penetrate into the stable layer capping the PBL. The warm air that mixes down as a result of entrainment causes the boundary layer to warm more rapidly, such that $\Delta_m\theta > 2\Gamma Q_0 t$, from which it follows that $h > \delta$. Without loss of generality we can express this by writing

$$h = \mathcal{A}\delta \,, \tag{32}$$

where $\mathcal{A} \geq 1$ measures the amount of entrainment.

The advantage of this prototype problem is that the paucity of parameters allows us to constrain A on purely dimensional grounds. In the Boussinesq limit the equations admit three fundamental dimensions (distance, time, and energy/temperature) and six parameters: $\Gamma, Q_0, t, g/\Theta$, as well as the molecular viscosity ν and thermal diffusivity κ. This leads to the identification of three non-dimensional numbers

$$\pi_1 = \frac{\nu}{\kappa}, \quad \pi_2 = (tN)^{1/3}, \quad \text{and} \quad \pi_3 = \left(\frac{t}{N^2}\right)^{2/3} \frac{\mathcal{B}}{\kappa} \,. \tag{33}$$

Here π_1 is the Prandtl number that is fixed by the fluid's material properties. Based on a subsequent interpretation of the energetics it is straightforward to show that π_2 can be interpreted as a ratio of the convective time scale in the boundary layer to that of gravity waves above the layer, while π_3 can be interpreted as the ratio of a convective time-scale to a diffusive timescale across the layer — effectively a Rayleigh number. Based on these considerations $\mathcal{A} = \mathcal{A}(\pi_1, \pi_2, \pi_3)$.

Because $\kappa/\mathcal{B}$ is typically much less than N^2, for $t \gg 1/N \approx 100$ s both π_2 and π_3 are much larger than unity. This motivates the assumption of complete similarity in π_2 and π_3; this is equivalent to saying that

$$\lim_{\pi_2,\pi_3\to\infty} \mathcal{A}\Big|_{\pi_1=\text{const.}} = A \,, \tag{34}$$

and that A is a universal $\mathcal{O}(1)$ constant. Physically we can think of A as measuring how deep a mixed layer, constrained to match the heat content in both the warmed layer and overall, must be. This interpretation is illustrated graphically in Fig. 7, where θ_m and h_m were calculated from an actual large-eddy simulation using the methods outlined above.

The entrainment constant A can be further constrained energetically. For instance, given h ,

$$\Delta_+\theta \equiv \theta_i(h) - \theta_m = \left(1 - A^{-2}\right) \frac{h\Gamma}{2} \,, \tag{35}$$

which defines the operator Δ_+ that measures a difference in the bulk value of a quantity and its value just above the PBL. An equivalent mixed layer growing at the same rate as the actual boundary layer is characterized by a heat flux that is linear with height and discontinuous at h. Its value at $h - \varepsilon$ can be obtained by integrating over the discontinuity, (*e.g.,* Lilly, 1968) such that

$$Q_{h_-} = -\Delta_+\theta \frac{dh}{dt} = Q_0(1 - A^2) \,. \tag{36}$$

Choosing $A^2 = 6/5$ yields the entrainment law, $Q_{h_-}/Q_0 = -1/5$, equivalently, $\mathcal{B}_{h_-}/\mathcal{B}_0 = -1/5$, that is frequently the basis of parameterizations. This relation can be expressed in terms of the

non-dimensional entrainment velocity, w_e, scaling with a bulk Richardson number, such that

$$\frac{w_e}{w_*} = \frac{\mu}{Ri} \quad \text{where} \quad Ri \equiv \frac{g\Delta_+\theta h}{\theta_0 w_*^2} \tag{37}$$

and $\mu = 1/5$. This is equivalent to a statement that the entrainment heat flux is a constant fraction of the surface flux,

$$w_e\Delta_+\theta = -\,\mu Q_0\,. \tag{38}$$

Furthermore, analogous to the encroachment relations in (31) and with reference to the mixed-layer sketch in Fig. 7, the penetrative-convection mixed-layer properties are the following:

$$\begin{aligned} h_m &= \left(\frac{2Q_0 t}{\Gamma}\right)^{1/2} \frac{1+\mu}{\sqrt{1-\mu}}\,, \qquad \delta_m = \frac{h_m}{1+\mu}\,, \\ \Delta_m\theta &= \left(\frac{2Q_0\Gamma t}{1-\mu}\right)^{1/2}, \qquad \Delta_+\theta = \mu\Delta_m\theta\,. \end{aligned} \tag{39}$$

That is, with penetrative convection the bulk temperature is warmer and the layer is deeper than with simple encroachment convection.

What is missing in this mixed-layer model is a characterization of the entrainment layer thickness, because it is idealized as a zero-thickness temperature jump at the top; however, a plausible extrapolation is that a self-similar evolution in the profile $\theta(z)$ will have all vertical lengths scale $\propto h_m(t)$, in particular it will be thinner when Γ is stronger.

In general, $\theta(z)$, or any material property for that matter, will not be discontinuous at h and the heat (equivalently buoyancy) flux at h will depend on the vertical structure of the boundary layer. That said, to the extent our similarity hypothesis is valid, then the particular profile of $\theta(z,t)$ must grow self-similarly in time (to do otherwise would imply a dependence on either π_2 or π_3) and hence the non-dimensional profile of θ must be universal; this means that the actual buoyancy flux at h, or the actual rate of change of θ over some distance at h, will be related by fixed constants (determined by the actual boundary layer structure) to the values determined for an equivalent mixed layer. The requirement that $\widehat{\mathcal{B}} > 0$ places an upper bound on A of $\sqrt{2}$.

Knowing the structure of the equivalent mixed layer buoyancy flux allows us to specify a velocity scale, w_* based on the dissipation rate, ε, of turbulence kinetic energy averaged across the layer. Doing so doing yields

$$w_* = A_\varepsilon\left[\widehat{\varepsilon} h\right]^{1/3} = A_\varepsilon\left[\widehat{\mathcal{B}} h\right]^{1/3}\,, \tag{40}$$

in the limit $dh/dt \ll w_*$, and with a vertical average over h denoted by the carat. Choosing $A_\varepsilon^3 = 2(2-A^2)^{-1}$ for the order unity prefactor yields $w_* = (\mathcal{B}_0 h)^{1/3}$ in the mixed layer limit. This velocity scale is analogous to w_f, discussed earlier to scale free convection in the surface layer. It was originally proposed by Deardorff (1970). Given w_* it is straight forward to define the turbulence timescale τ_* and a turbulent temperature $\theta_* = Q_0 w_*^{-1}$. The latter allows us to define an effective Rayleigh number,

$$Ra \propto \frac{g h^3 \theta_*}{\Theta_0 \nu\kappa} = \frac{B_0^{2/3} h^{8/3}}{\nu\kappa} = \frac{\pi_3}{\pi_1}\left(2A^2\right)^{4/3}\,, \tag{41}$$

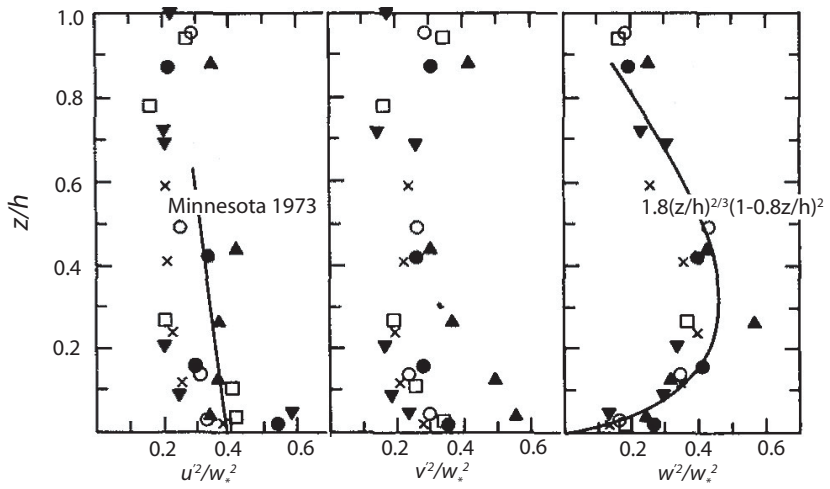

Figure 9: Convective, or mixed-layer, scaling of convective layer variance budgets (Lenschow *et al.*, 1980).

from which our interpretations above of π_2 and π_3 originate.

The convective (or mixed-layer) scaling used to non-dimensionalize the mean PBL structure can, in analogy to the treatment of the surface layer, also be used to non-dimensionalize higher-order moments through the mixed layer. For example, Fig. 9 demonstrates the ability of convective layer scaling to collapse the variance profiles of u, v and w over the depth of many convective layers, with h varying by a factor of three, and w_* varying by a factor of 2.5. The tendency for $\overline{ww}/(w_* w_*)$ to peak at a value between 0.4 and 0.5, roughly a third of the way up in the PBL is also evident in simulations and convection tank experiments, and is a hallmark of turbulence in convective PBLs.

Convective Layer Momentum Budgets In the presence of a weak interior flow, $\mathbf{U_g}$, the mean velocity profile must still satisfy the momentum balance equations. In a CBL $\mathbf{U}$ is assumed to be uniform in the mixed layer, with $\overline{\mathbf{u}'_h w'}$ linearly proportional to z. The eddy fluxes at the top of the mixed layer are assumed to be related to velocity differences across the entrainment layer, somewhat analogous to the heat-flux relation in (36), *e.g.,*

$$\overline{u'w'}(z_i) \;=\; -w_e(U_g - U)\,, \qquad \overline{v'w'}(z_i) \;=\; -w_e V_g\,, \tag{42}$$

where we now have oriented the axes such that $V = 0$ in the mixed layer (hence the surface stress is only in the $\hat{\mathbf{x}}$ direction, with $\overline{u'w'}(0^+) \;=\; -u_*^2$). Using this in the PBL momentum budget, we obtain integral relations for the CBL momentum balances,

$$-w_e(U_g - U) + u_*^2 \;=\; -fhV_g \tag{43}$$

$$-w_e V_g \;=\; fh(U_g - U)\,. \tag{44}$$

We can solve these exactly given u_* and w_e, and the latter can be obtained from w_* and Ri_{cbl} by (37).

A particularly simple solution arises if we make the approximation, $Ro_e = w_e/fh \ll 1$[3], *viz.,*

$$\frac{U_g - U}{u_*} = -Ro_e \frac{V_g}{u_*} = Ro_e \frac{u_*}{fh} + \mathcal{O}(Ro_e^2) \tag{45}$$

$$\frac{V_g}{u_*} = -\frac{u_*}{fh} + \mathcal{O}(Ro_e^2). \tag{46}$$

Thus, $V_g < 0$ and $U_g > U$ here, with $U^2 < U_g^2 + V_g^2$. Since the mixed layer velocity is in the $\hat{\mathbf{x}}$ direction, the turning angle can be defined by

$$\tan[\beta] = -\frac{V_g}{U_g} \approx \frac{u_*}{U_g}\frac{u_*}{fh}, \tag{47}$$

and β is often small. In particular, for $U_g = 10$ m s^{-1} and the other values mentioned previously, a typical value is $u_* = 0.5$ m s^{-1}, hence $\beta \approx 14^o$. This β value is much less than that found in the non-convective Ekman PBL, where $\beta \approx 30^o$ in the turbulent regime or 45^o in the laminar regime (*i.e.,* with constant eddy viscosity).

Transport Asymmetry: We can consider three types of scalar fields in the CBL: the *active scalar* b that is forced in a destabilizing way by the flux at $z = 0$ and in a partly compensating, stabilizing way at $z = h$ due to the inversion; a passive scalar being transported from the interior *towards the boundary* (sometimes called "top-down" when the boundary is at the bottom) where the surface flux is zero; and a passive scalar being transported *away from the boundary* (*i.e.,* "bottom-up") because of a flux at $z = 0$. Remarkably, each of these has a different transport structure, as expressed in terms of an eddy diffusivity, $\kappa_e(z)$. The cause of this asymmetry is in the driving at the flow, where the bottom-up flux is destabilizing while the top-down buoyancy flux stabilizes the flow (*cf.,* Rayleigh-Benard convection where both boundary fluxes are destabilizing). As a result it is not surprising that transport away from the boundary — in association with rising buoyant plumes — is more efficient by this measure than towards it, by a factor of 2-3. These are sketched in Fig. 10.

A further consequence of this asymmetry is that the active scalar diffusivity even becomes singular for the buoyancy flux in the middle of the layer where $d\bar{b}/dz$ changes sign and $\overline{w'b'}$ does not (further discussed in Sec. 6). Also, since $K_m(z) \leq 0.1 w_* h$, an eddy Prandtl number, $Pr_e = K_m/K_h$, is < 1 for all three types of scalars. Because of the combination of the surface flux and the entrainment-layer flux, the vertical profile of buoyancy flux can be view as a superposition of top-down and bottom-up scalar transports.

Because of this variety of behavior, we must conclude that local eddy diffusion is not a fundamentally correct characterization of turbulent transport in the CBL, hence a more non-local description is required (*i.e.,* one incorporating knowledge of the surface fluxes and interior gradients and permitting finite turbulent fluxes at levels with zero or reverse-sign mean gradient). The circulation pattern underlying the non-local transport, of course, is the coherent plumes. The plume dynamics control the vertical profiles of variance and skewness for turbulent vertical velocity in

[3]To illustrate this for an atmospheric CBL, consider the following numerical values: $\mathcal{B} = (g/T_o)(100$ W m$^{-2})/(\rho c_p = 10^3$ J m^{-3} K$^{-1}) = 3^{-3}$ m^2 s^{-3}, $h = 10^3$ m, $w_* \approx 1$ m s^{-1}, $w_e \approx 0.01$ m s^{-1} (*i.e.,* ≈ 1 km day^{-1}), $f = 10^{-4}$ s^{-1}, $w_*/fh \approx 10$, $Ro_e \approx 0.1$.

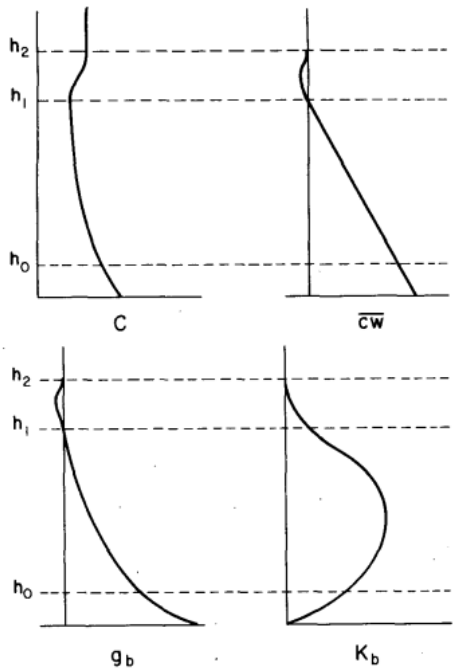

FIG. 4. Profiles in bottom-up diffusion: (upper left) mean mixing ratio; (upper right) scalar flux; (lower left) dimensionless mean gradient; (lower right) eddy diffusivity.

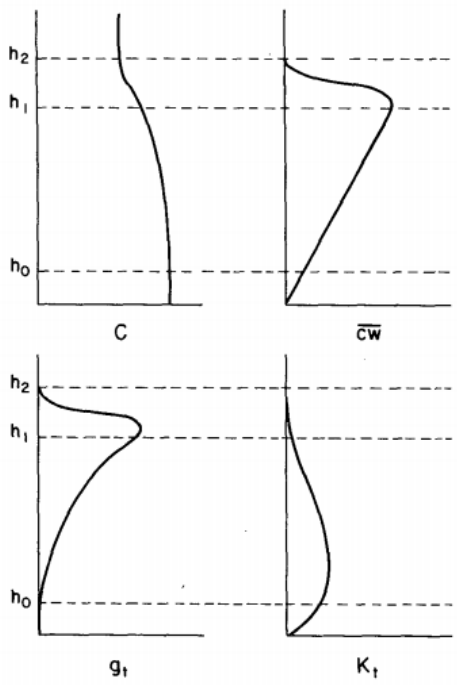

FIG. 5. As in Fig. 4, but for top-down diffusion.

Figure 10: Sketches of the mean and eddy flux profiles, the mean gradient, and the diagnosed eddy diffusivity for scalar fields in a convective atmospheric boundary layer: (left) bottom-up transport from surface flux and (right) top-down transport from entrainment flux. (Wyngaard and Brost, 1984)

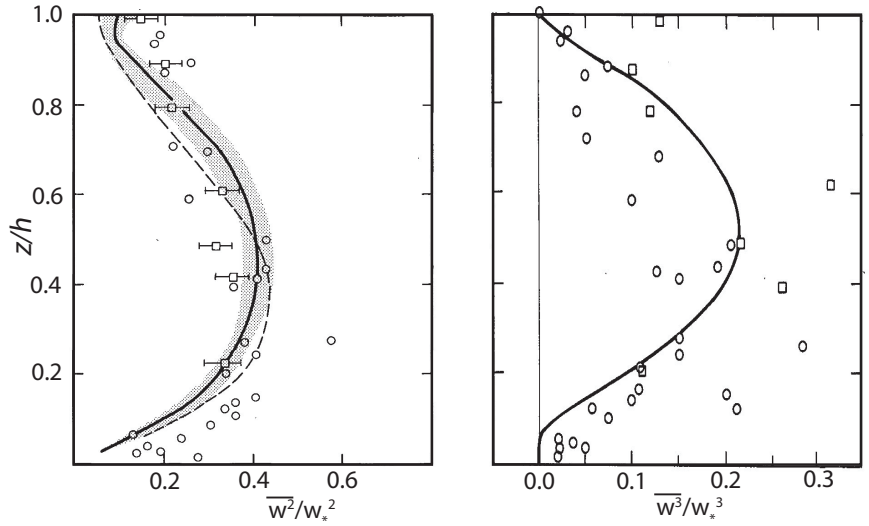

Figure 11: Convective, or mixed-layer, scaling of convective layer variance budgets (Moeng and Wyngaard, 1989). Left panel: Variance from $(96)^3$ LES (solid curve), $(40)^3$ LES (dashed curve), AMTEX (circles, *e.g.,* previous figure) and convection tank experiments (open squares). Right panel: Vertical velocity skewness from LES (solid line).

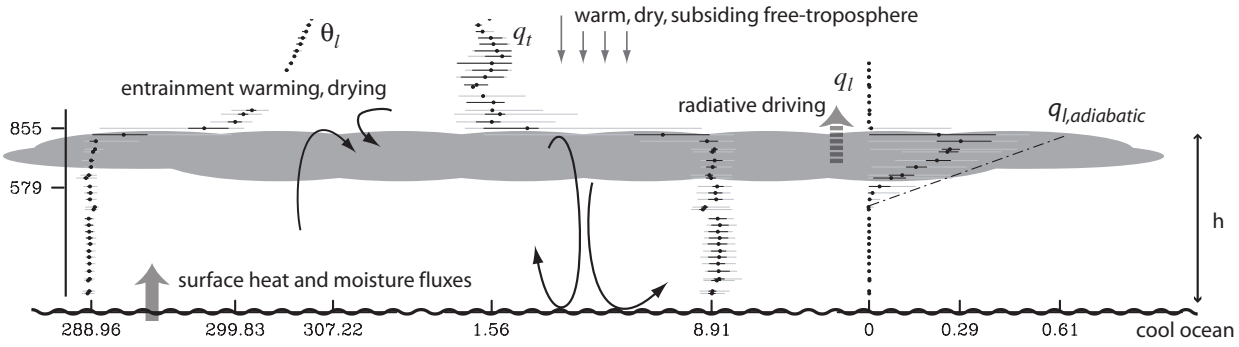

Figure 12: Schematic of stratocumulus topped boundary layer

the CBL (Fig. 11). The maximum in $\overline{w'^2}(z)$ below the mid-plane is due to the acceleration near the boundary where the buoyancy anomaly is created and the deceleration into the entrainment layer where stable stratification is encountered, and the mid-level maximum in skewness reflects the intense updrafts inside the narrow plumes relative to the weaker downdrafts in the broader region outside them. The decay of $\overline{w'w'}$ as z approaches h is accompanied with a general decay in turbulence throughout the PBL as the capping inversion limits the extent of turbulence production and turbulence over all.

h/L	Regime
$h/L > 0$	stable boundary layer
$h/L \approx 0$	neutral (or Ekman when $f \neq 0$), layer
$-1 < h/L < 0$	shear dominated, but weakly convective
$-10 < h/L < -1$	convection with shear
$h/L < -10$	free convection

Table 2: Boundary Layer Regimes.

Most boundary layers are neither purely convective, nor are they neutrally stratified shear layers. To quantify the various intermediate states boundary layers are often classified according to h/L. Here h is non-dimensionalized by L because the overall buoyancy production in the boundary layer scales with h, consequently h/L is a better measure of the overall stability of the boundary layer. Such a classification scheme leads to the definition of different regimes as shown in Table 2. The regimes are often associated with varied phenomena, for instance for $-10 < h/L < -1$ convective rolls are often found in the boundary layer, while plumes or thermals are found at more negative values of h/L. PBL regimes where $h/L \geq 0$ are discussed in Sec. 3 below.

2.2 Stratocumulus-Topped Boundary Layers

There are frequent associations between clouds and the convective boundary layer in the atmosphere, for the obvious reason that overturning motions can bring moist air to a condensation level (Stevens, 2005).

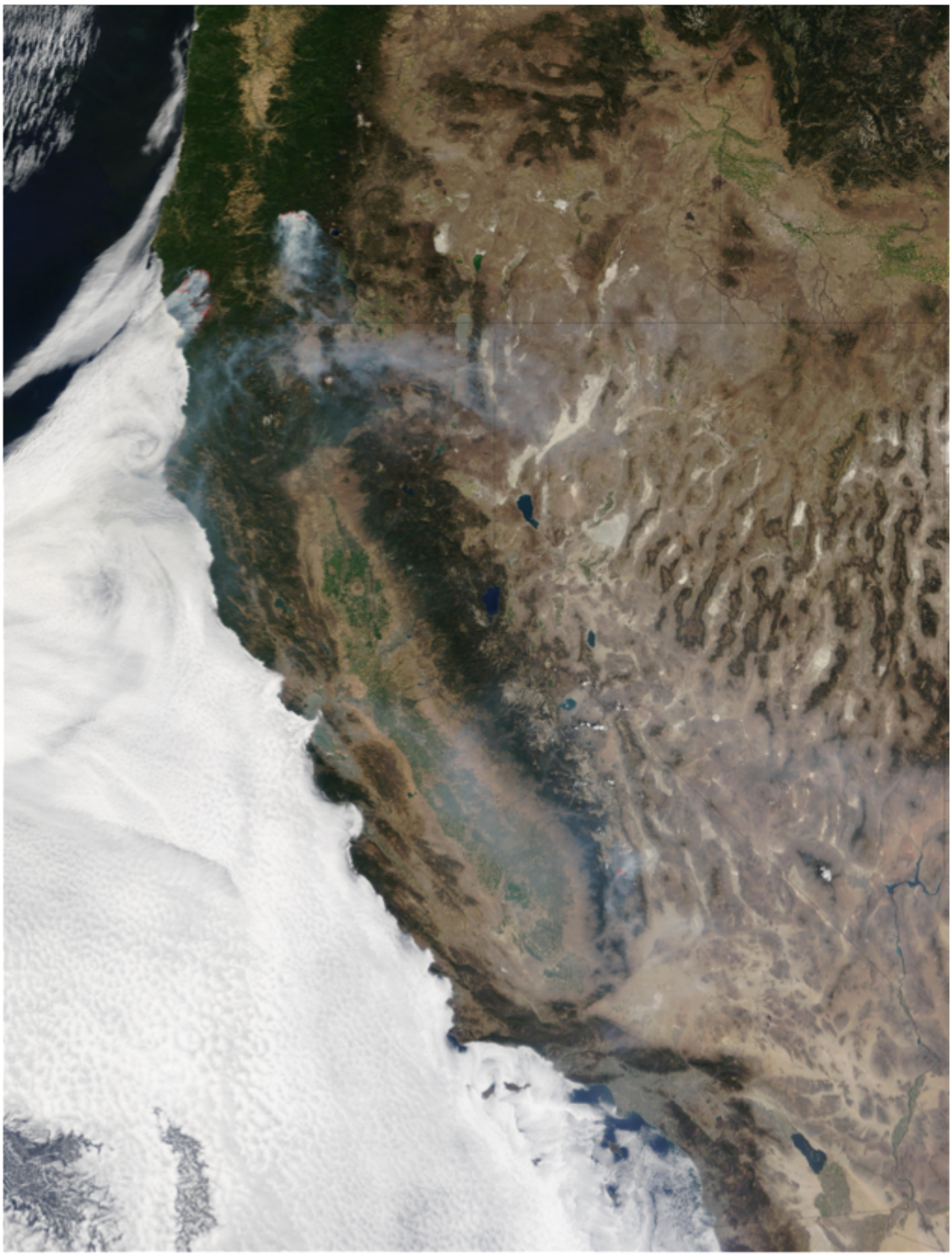

Figure 13: Because of the cold ocean surface in the California Current System (due to coastal upwelling of cold interior water) and the generally descending air aloft (part of the atmospheric Hadley circulation), there are commonly dense decks of low-level stratus clouds, which reduces the solar heating of the ocean. Locally this is called “June gloom” or “May gray”, except that now it seems to be starting in March.

In some situations where very stable boundary layers might be expected, clouds develop and act to help destabilize the layer. Stratocumulus, for instance, are common in regions where the lower-tropospheric stability, as measured by the difference between the potential temperature in the free atmosphere (typically at 700 hPa) and its value at the surface, is very large. However given an adequate supply of surface moisture, this stability can limit entrainment mixing, and hence drying, leading to the development of a shallow cloud layer at the PBL's top. This opacity of the cloud layer at infrared wavelengths acts to concentrate strong radiative cooling in a thin (tens of meters) layer at the top of the cloud. The air cooled at the top of the cloud becomes convectively unstable and promotes the overturning of the layer. Especially at night when the radiative cooling is not offset by solar heating, cloud-top cooling can be an effective driver of turbulence resulting in well-mixed cloud-topped boundary layers. An example, based on observations during the DYCOMS-II field program, is in Figs. 12-13.

In Fig. 12 the marine boundary layer is a well-mixed, cool, and moist layer, capped by a much warmer and drier free troposphere. The cloud topping this layer has water content that is nearly adiabatic, *i.e.,* equal to what would be expected for parcels lifted reversibly from the sub-cloud layer. The figure also shows that the strength of the capping inversion is strong compared to the fluctuations of quantities within the PBL (shown in the observational data points by the whiskers that span the entire range) indicative of the fact that entrainment (mixing with the free troposphere) is weak. For typical stratocumulus-topped mixed layers, the radiative driving of turbulence is the primary source, although it may be somewhat influenced by modest fluxes of heat and moisture at the surface.

Because the stratocumulus-topped PBL critically involves the change of phase of moisture, its description benefits from the use of variables that are conserved under this process. Examples are the total water specific humidity q_t for moisture and either a moist entropy (such as the equivalent potential temperature), or a moist static energy for temperature. An example of the latter is

$$s_l = c_p T + gz - L q_l \ , \tag{48}$$

which is called the liquid water static energy. Here L is the enthalpy of vaporization, q_l is the liquid water specific humidity, and other variables have their traditional meanings. Because the vertical structure of the stratocumulus-topped boundary layer is typically simple, the first-order question is what controls its bulk properties. To investigate this we integrate the conservation laws for moisture and s_l to some height h_+ just above the top of the turbulent boundary layer, and if we denote a vertical average of a quantity by a hat, then the evolution of the mean mass, liquid-water static energy and moisture are described as follows,

$$\frac{D}{Dt} h = \overline{w}_+ + E \tag{49}$$

$$\frac{D}{Dt} \hat{s}_l = \hat{R}_s + \frac{1}{h} \left[V(s_{l,0} - \hat{s}_l) + E(s_{l,+} - \hat{s}_l) \right] \tag{50}$$

$$\frac{D}{Dt} \hat{q}_t = \hat{R}_q + \frac{1}{h} \left[V(q_{t,0} - \hat{q}_t) + E(q_{t,+} - \hat{q}_t) \right] \ . \tag{51}$$

Here V parameterizes the surface fluxes, E parameterizes the entrainment rate, and R denotes a diabatic process, for instance radiative fluxes acting on s_l or precipitation acting on q. To close the system it is assumed that R, V, and E are functions of the state of the system. Given an assumption

about the layer's vertical structure, it is straightforward to use M-O theory to estimate V. In the absence of drizzle, knowledge of the state of the system is sufficient to determine R based on the principles of radiative transfer, hence all that remains is to specify E.

The dynamics of this system are relatively simple to understand in some limiting circumstances. For instance a minimal representation of stratocumulus consists of a horizontally homogeneous, non-precipitating layer with V fixed to some specified value, E modeled as discussed subsequently, and a radiative driving

$$R_s = -\partial_z F \Longrightarrow h\hat{R}_s = F_0 - F_+ \equiv -\Delta F \ . \tag{52}$$

Here, and subsequently, $\Delta\phi$ is used to denote $\phi_+ - \phi_0$, where ϕ is arbitrary. Although ΔF is related to the structure of the layer, for our immediate purposes we can consider it constant. For sufficiently thick clouds (more than 100 m deep) at night this is not a particularly limiting assumption. With these assumptions the mixed-layer equations can be written as a system of three ODEs:

$$\frac{d}{dt}h = \overline{w}_+ + E \tag{53}$$

$$\frac{d}{dt}\hat{s}_l = \frac{1}{h}\left[-\Delta F + V(s_{l,0} - \hat{s}_l) + E(s_{l,+} - \hat{s}_l)\right] \tag{54}$$

$$\frac{d}{dt}\hat{q}_t = \frac{1}{h}\left[V(q_{t,0} - \hat{q}_t) + E(q_{t,+} - \hat{q}_t\right] \ . \tag{55}$$

The model of E is crucial. For now we consider a simple, physically plausible relation that simplifies the analysis, *viz.,* the case when

$$E = \alpha\Delta F/\Delta s_l \ , \tag{56}$$

where α is a constant of order unity. Heuristically this expression for E suggests that the entrainment rate is proportional to the rate of driving of the flow (as measured by R_s) and inversely proportional to the stability of the interface at cloud top, as measured by Δs_l. Δq measures the jump in q at the BL top (Fig. 12). Closures that more faithfully respect the energetics of the system account for the uncertain stability of the cloud top layer across which radiative cooling, phase changes, and mixing all effect the density in uncertain ways.

With (56), as a model for E the steady states of the system (which we denote by subscript '∞') are as follows:

$$h_\infty = h_0\left(\frac{\alpha}{1+\sigma-\alpha}\right) \tag{57}$$

$$s_\infty = s_0 - \Delta s\left(\frac{1-\alpha}{\sigma}\right) \tag{58}$$

$$q_\infty = q_0 + \Delta q\left(\frac{\alpha}{1+\sigma}\right) \ , \tag{59}$$

where

$$h_0 = \frac{V}{D} \quad \text{and} \quad \sigma = \frac{V\Delta s}{\Delta F} \ . \tag{60}$$

The height-scale h_0 measures the height the equilibrium boundary layer would obtain for $\alpha = \sigma = 1$. In the stratocumulus regions, $\mathcal{D} \approx 1 \times 10^{-5}$ s^{-1} and $V \approx 0.01$ ms^{-1} yielding values of

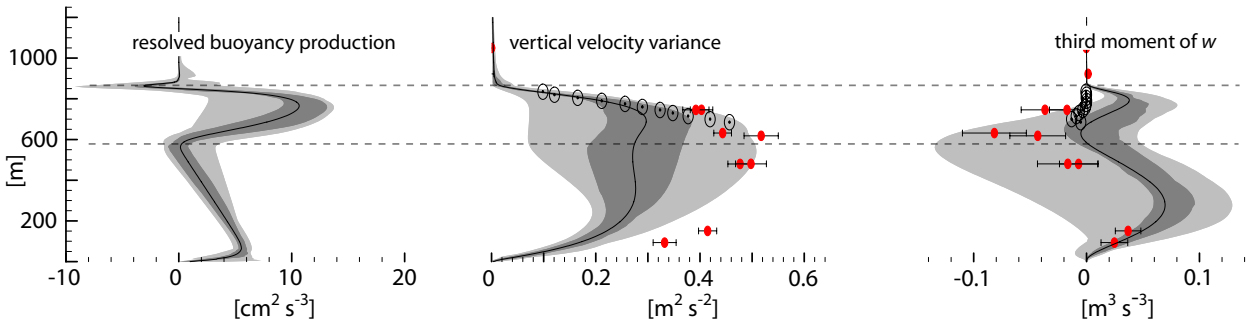

Figure 14: Turbulence production by buoyancy, vertical velocity variance and skewness for LES (shaded) of the stratocumulus topped boundary layer. Symbols denote observed variances and skewness. The shading reflects the spread among an ensemble of 18 LES, with the darkened area showing the inter-quartile spread and the light shading showing the full range. (Stevens *et al.*, 2005)

$h_0 \approx 1$ km. Similarly for a radiative flux divergence of 100 Wm^{-2} and $\Delta s \approx 10^4$ J kg^{-1} we can expect $\sigma \approx 1$. By inspection we see that α is critical to the balances of mass, heat and moisture. Large α corresponds to deeper PBLs that are warmer and drier, while small α provides no basis for deepening the PBL against the countervailing force of large-scale subsiding motion. For $\alpha > 1$ (super entrainment), processes other than radiative driving are important to the entrainment rate, $s_\infty > 0$, and hence heat fluxes are into the surface ocean.

Energetics: Before addressing the energetics it is worthwhile to introduce the important concept of quasi-stationarity. We say that a flow is quasi-steady when a conserved scalar ϕ (*i.e.,* one where R_ϕ vanishes) has linear fluxes. To see this, recall that for a horizontally homogeneous flow, an advected scalar ϕ satisfies the equation,

$$\partial_t \overline{\phi} = -\partial_z \overline{w'\phi'} \,, \tag{61}$$

so linearity of the fluxes means that $\partial_t \partial_z \overline{\phi} = 0$. Thus the shape of the $\overline{\phi}$ profile is not changing with time when the fluxes are linear. This motivates the descriptive word "quasi-steady." Whereas, the boundary layer flows only approach equilibrium on long timescales and are set by the mean flow; they generally approach quasi-steady states on the timescales of the turbulent quantities that we shall later show are typically minutes to tens of minutes. This idea of quasi-stationarity places important constrains on the fluxes that can be quite useful for a number of purposes.

For the case when h is the only length-scale, we can posit the existence of a velocity scale w_* that non-dimensionalizes the dissipation, such that

$$\varepsilon \left(\frac{h}{w_*^3} \right) \tag{62}$$

is universal. In equilibrium (62) implies that in the limit $E/w_* \ll 1$

$$w_*^3 \propto C_\epsilon \int_0^{h+} \mathcal{B} dz \,, \tag{63}$$

where the constant of proportionality is typically specified as $5/2$; this definition of w_* corresponds to the velocity scale, $w_* = (\mathcal{B}_0 h_+)^{1/3}$, that Deardorff introduced to scale the dry convective boundary layer. The velocity scale (63) is often used to scale a stratocumulus topped boundary layer, although, as we might anticipate (discuss further shortly), the assumption that h is the only length-scale in the problem is much less justified.

Given a length-scale h and the velocity scale w_* we can define a turbulent timescale $t_* = h/w_*$. Because w_* is typically near unity, this $t_* \approx 10 - 20$ minutes for typical boundary layer depths. It is on this timescale that one expects boundary layers to approach quasi-steady states. In so far as changes to the forcings occur on timescales much larger than t_*, quasi-steadiness is a good assumption.

An example of stratocumulus energetics is given in Fig. 14 showing an ensemble representation of the energetics of an observed case of stratocumulus. The spread among the various LES is large, reflecting differences in the entrainment rates produced by different simulations arising from the difficulty of representing the energetics at what amounts to a very sharp, and poorly resolved, entrainment interface at cloud top. Those simulations that tend to entrain the least have the greatest buoyancy production by turbulence, the largest turbulence activity, and are most negatively skewed, reflecting the downdraft dominance in the radiatively-driven layer that, on the whole, most of the LES do not represent very well compared to the measured negative skewness in this thin entrainment layer. An interesting aspect of this figure is the large increase in the buoyancy in the cloud layer. This is due to the way that fluctuations in the state parameters project onto the buoyancy. In the cloud layer, buoyancy fluctuations are dominated by fluctuations in q_t, while in the sub-cloud layer buoyancy fluctuations are mostly driven by fluctuations in s_l. This illustrates the important energetic role of the depth of the cloud layer, and hence the non-universality of w_* as described above. It can also lead to interesting phenomena, such as the cloud layer doing work on the sub-cloud layer, effectively, moisture fluxes driving reverse heat fluxes.

2.3 Cumulus-Topped Boundary Layers

Cumulus clouds often top convective boundary layers over the ocean in regions where the lower tropospheric stability is insufficiently large to trap the moisture in a thin layer. These clouds act to vent the sub-cloud layer of mass and moisture. For most practical purposes, the sub-cloud layer of a cumulus topped PBL is thought to be similar to that of a dry convective PBL, although the turbulence and energetics of the cloud layer is considerably more complex.

3 Neutral and Stable Boundary Layers

3.1 Ekman Layer

A paradigm for neutral, or unstratified, PBLs is the turbulent Ekman layer. This is thought to differ in at least two fundamental ways from the classical Ekman layer discussed in *Shear Turbulence*. First, the turbulence does not provide a constant eddy viscosity. Second, there is almost always a capping inversion that demarcates the vertical extent of the PBL and provides a rather sharp interior boundary to the mean shear and turbulent variance and flux profiles.

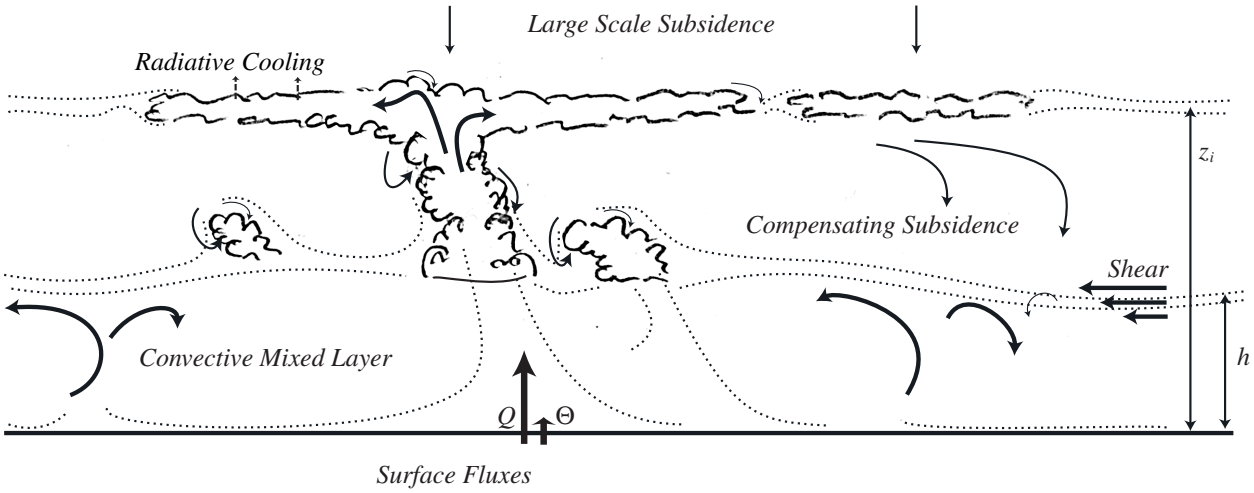

Figure 15: Schematic of cumulus-topped boundary layer based on simulations and observations during ATEX. (Stevens *et al.*, 2001.)

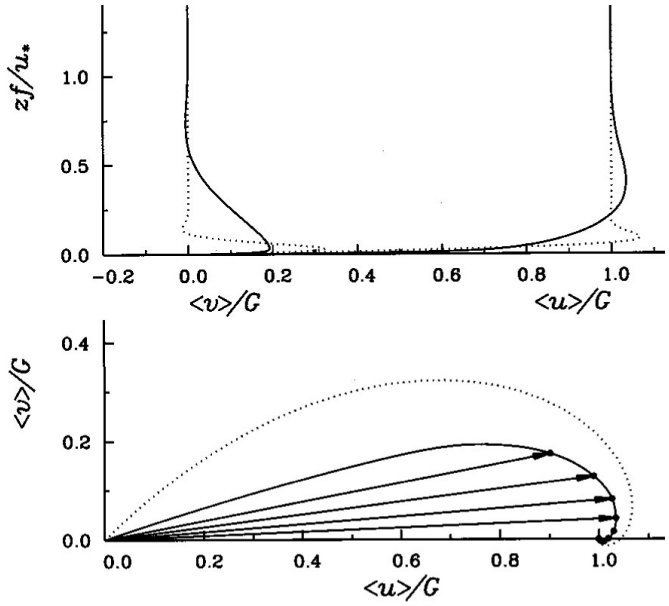

Figure 16: Numerical simulation of a turbulent Ekman layer. Dotted lines are for the laminar solution; solid lines are for turbulent flow at $Re = 1000$. Upper panel: Mean velocity on axes aligned with the geostrophic wind. Lower panel: Hodograph, with vectors showing mean velocity at zf/u_* = 0.1, 0.2, 0.3, and 0.4. (Coleman, 1999)

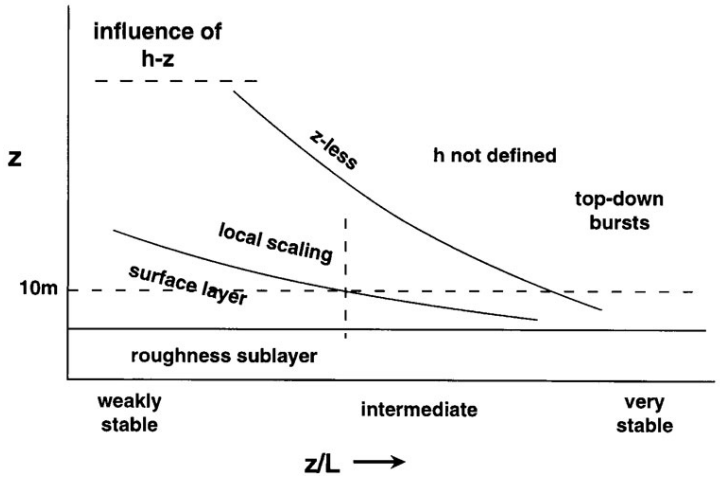

Figure 17: Schematic of stable boundary layer regimes. The surface layer has Monin-Obukhov similarity, the "local" layer has a z similarity scaling with the Ozmidov length $L_O(z)$. Above the local layer there is no similarity scale (*i.e.,* "z-less"). For weakly stable conditions the distance to the top at $z = h$ may be relevant. Very stable layers have ill-defined tops and an amorphous transition into the interior regime. (Mahrt, 1999)

For idealized flows, wherein an externally imposed stratification does not set the depth of the PBL, we can investigate the effects of turbulence on the developing Ekman layer through numerical simulation. Figure 16, taken from direct numerical simulations by Coleman (1999), shows that the turbulent Ekman layer has a less pronounced Ekman spiral than the laminar solutions with the turning angle for the near-surface wind, $\approx 29^o$, as compared to 45^o, and the depth of the layer of $\mathcal{O}(u_*/f)$. The eddy viscosity profile, $K_m(z)$, (not shown) increases from zero (as we expect in a turbulent shear layer) near the surface, peaks in the middle of the PBL, and tends to decrease into the interior (though not sharply in this situation without a capping inversion) scale for the turbulent solutions

The analytic Ekman layer solution (*Shear Turbulence*) shows that h is finite in equilibrium in a uniform density fluid with rotation. When h is less than $\mathcal{O}(u_*/f)$, either because of a stable inversion or because the latter depth is diverging near the equator, the shear-driven PBL will always be developing (*i.e.,* continuing to deepen). Often, however, this rate of deepening is quite slow on the scale of an energetic eddy turn-over time, h/u_*, and, on any long time scale of many days, buoyancy forcing is not negligible, so that a purely shear-driven solution is not relevant to nature.

3.2 Stable Boundary Layer

A good overview of the stable boundary layer (SBL) is provided in Fig. 17. Further illustration of the influence of $\mathcal{B}$ on the shear PBL is given in Fig. 18, based on observations during a diurnal cycle in the atmosphere, where the afternoon convective layer, the CBL with $\mathcal{B} > 0$, is much deeper and has its $\mathbf{U}(z)$ more uniform with height (*i.e.,* showing a less pronounced Ekman spiral) than the evening stable layer, the SBL with $\mathcal{B} < 0$. The stabilizing buoyancy flux at the surface extracts energy from the turbulence generated by shear production (in addition to ϵ), it makes h smaller, it provides a stable stratification through the actively turbulent layer, and it makes the

turbulent eddies smaller (even when rescaled by the smaller h) because of $N^2 > 0$. Also, it throws the momentum equation,

$$\frac{\partial U}{\partial t} - f(V - V_g) \;=\; -\frac{\partial \overline{w'u'}}{\partial z}\,, \tag{64}$$

out of balance at levels previously within the PBL when the Reynolds stress collapses through TKE dissipation; this has the effect of generating inertial oscillations in this residual layer, which are related to the frequent occurrence of a *nocturnal jet* near $z = h$ in a stable PBL (Fig. 18). Another view of this transition from a CBL to a SBL is shown in Fig. 20, where the drop in u_* is partly due to a change in U_g as well.

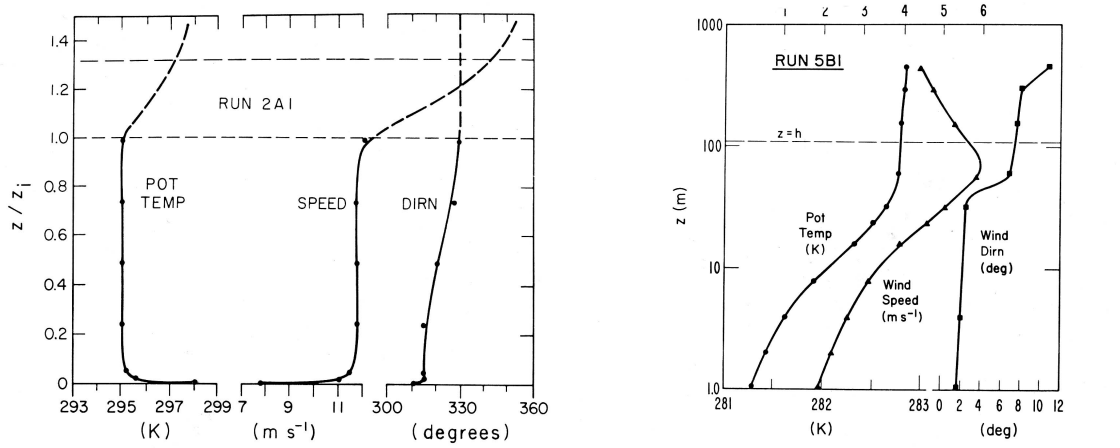

Figure 18: (Left) Early afternoon profiles of mean wind and potential temperature in the 1973 Minnesota experiment, *i.e.,* during a convective period. This moderately convective PBL had $h = 1250$ m and $h/L \approx -30$ (Kaimal *et al.*, 1976). (Right) Early evening profiles of mean wind and potential temperature in the 1973 Minnesota experiments, *i.e.,* after the transition to a stable period (Caughey *et al.*, 1979).

Large Eddy Simulations (LES) are more difficult for the SBL than for the CBL or neutral Ekman layer because of the very fine spatial scales that occur near its top where the $N^2(z)$ is large and the turbulence is weak and especially intermittent as $Ri(z)$ goes crosses a critical value. The mean profiles show stable stratification and shear throughout the layer (*i.e.,* it is not a mixed layer; Fig. 21). The energy cascade is, of course, forward in a boundary layer, and it exhibits an energy inertial range shape, anisotropically at larger scales and isotropically at smaller ones (Fig. 21). Its coherent structures are manifested as tilted temperature fronts in the downstream-vertical plane (Fig. 23) and hairpin vortices qualitatively elongated in the same plane and broadly similar to those seen in uniform-shear or shear boundary-layers (Fig. 24).

The range of actively turbulent scales of motion is squeezed in the *remnant layer* above the SBL, between the Ozmidov and Kolmogorov scales (*i.e.,* $L_O = (\epsilon/N^3)^{1/2}$ and $L_K = (\nu^3/\epsilon)^{1/4}$), much the same as seen previously in stratified turbulence. This is illustrated in Fig. 25 for the diurnal cycle in the upper ocean. Note that the range of scales shrinks once the transition to a SBL occurs, due to the decay of turbulence, hence the decrease in ϵ. There is also a strong coupling between the decaying 3D turbulence in this layer and internal gravity waves, since the eddy turnover time, $\tau_L = \epsilon^{-1/3} L^{2/3}$, at the top of the inertial range, $L = L_O$, is the same as a

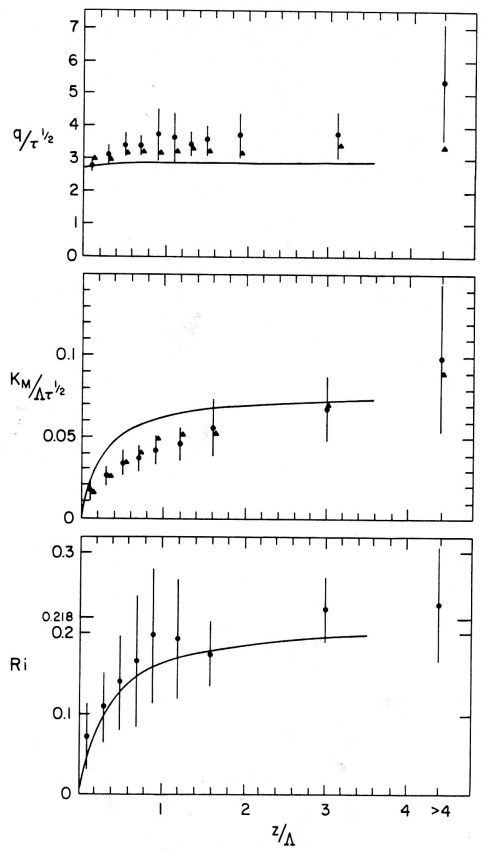

Figure 19: Some observed statistics from the nocturnal PBL (data points) and theoretical predictions from Nieuwstadt (1984). Abscissa is $\zeta = z/L$. Plotted are TKE scaled with the friction velocity (top), non-dimensional eddy viscosity, ν_e/u_*L (middle), and $Ri(z)$ (bottom).

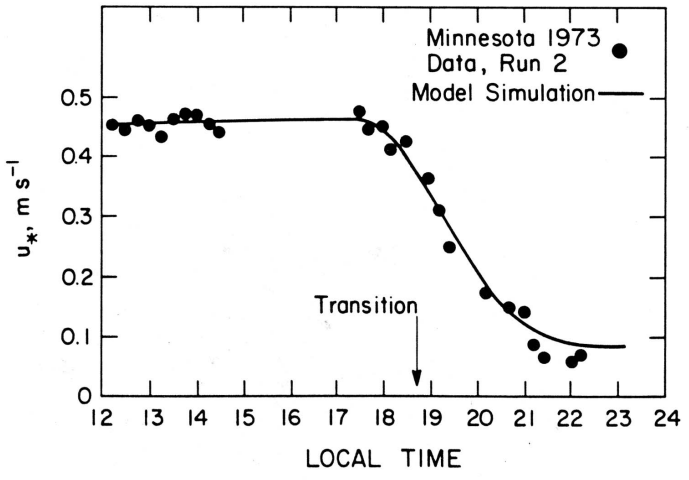

Figure 20: The late-afternoon decay of friction velocity u_* in the 1973 Minnesota experiment. (Wyngaard, 1975)

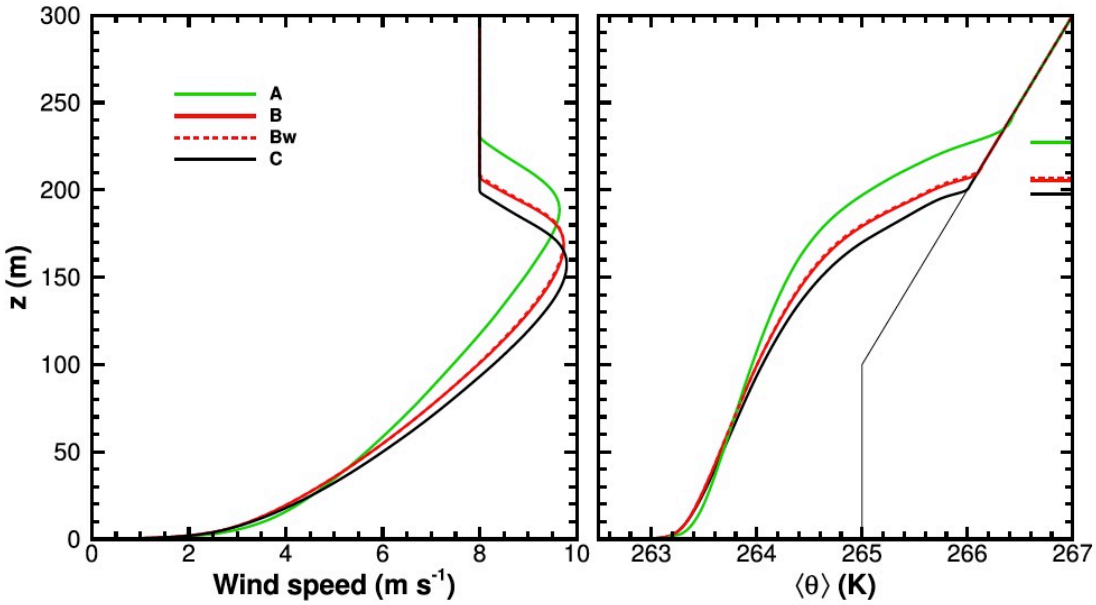

Figure 21: Mean vertical profiles in LES of the SBL. These are shown as functions of vertical resolution, (A,B/Bw,C) = (2,0.8,0.4) m, which is notoriously demanding to adequately resolve the entrainment at the layer top. Notice the persistent stable stratification in spite of the turbulent mixing and the "nocturnal jet" near the top (also seen in Fig. 18, right). (Sullivan *et al.*, 2016)

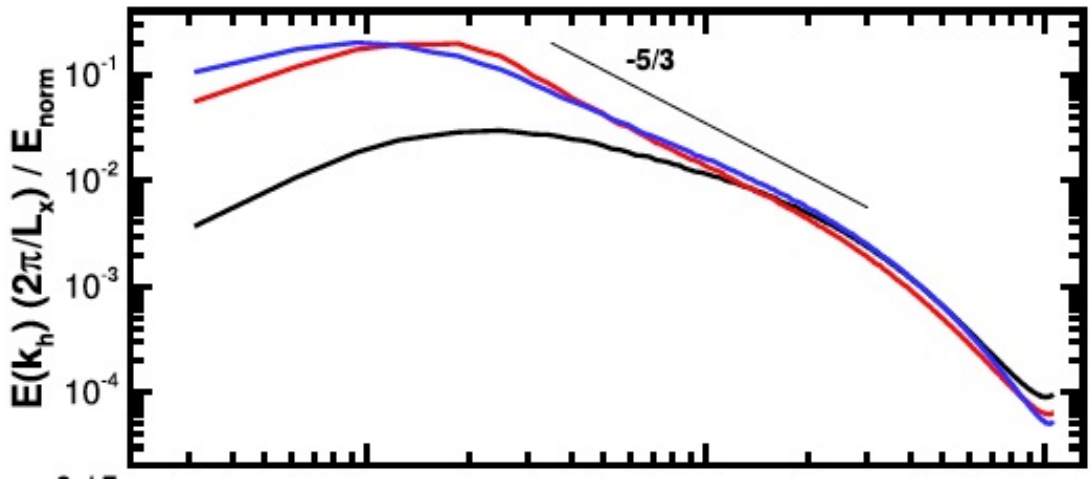

Figure 22: 2D horizontal wavenumber spectra for T (blue), (u, v) (red), and w (black) at a height $z = 0.2h$. Notice the $k^{-5/3}$ shape, broadly in T and (u, v), and only at smaller scales in w, indicating isotropy there. (Sullivan *et al.*, 2016)

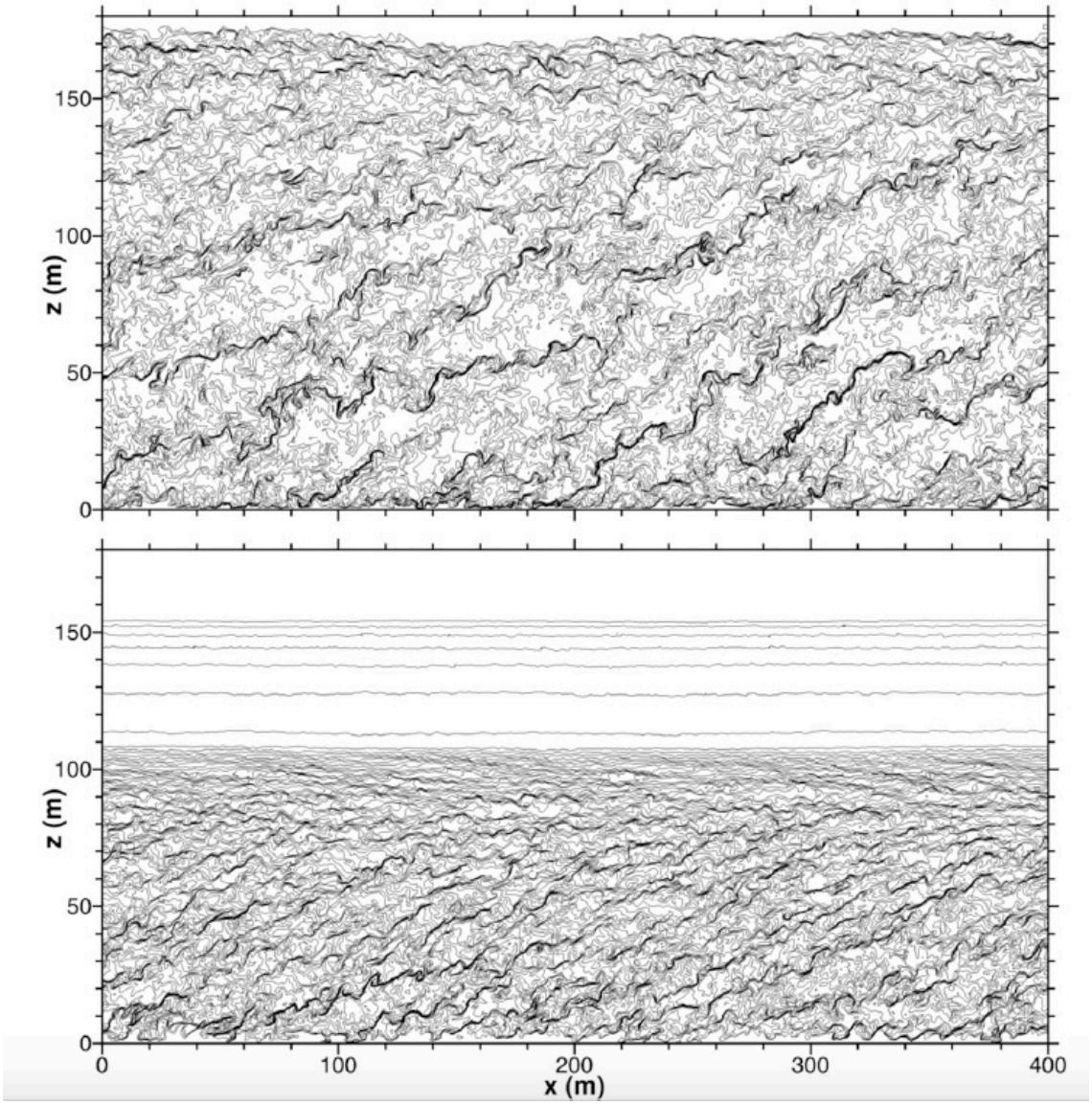

Figure 23: Contours of $T(x, z)$ for a given y from a LES of the SBL. The top panel has $h/L = 1.7$ and the bottom panel has $h/L = 6.0$. Temperature "fronts" or "ramps" are evident, and their tilt angle is reduced with stronger stratification. (Sullivan *et al.*, 2016)

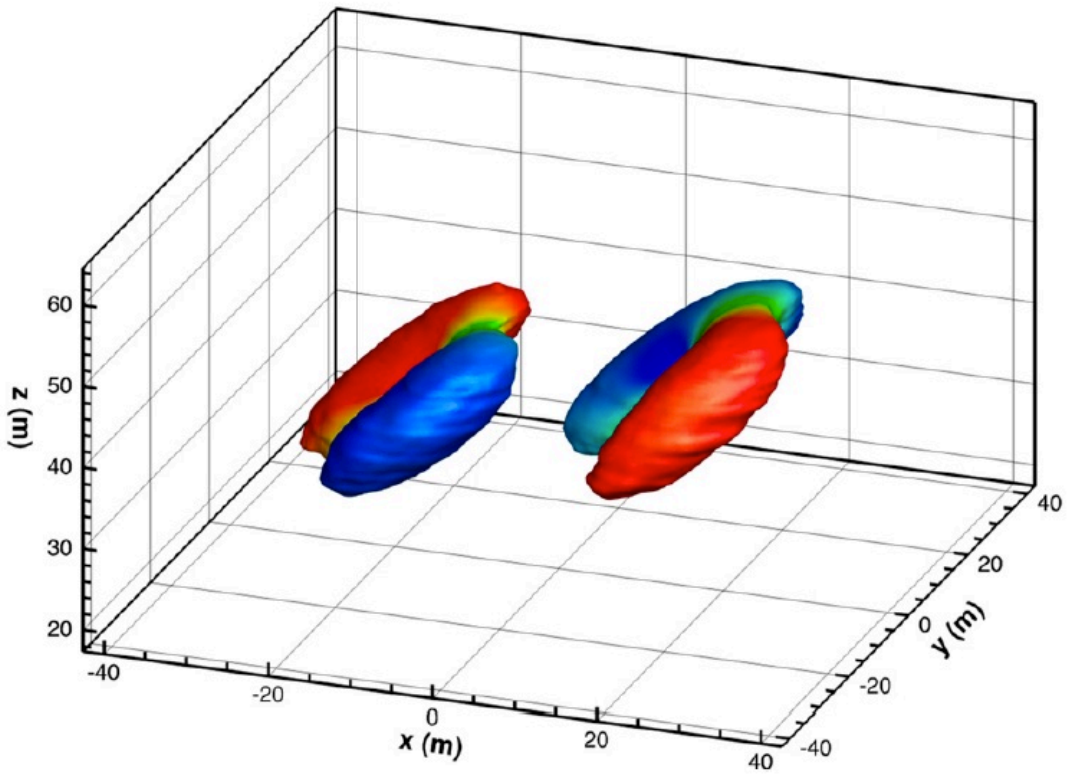

Figure 24: Oblique view of the typical 3D vortical structure in a SBL LES. This is based on conditional averaging of "strong events" at a height of $z = 0.2h$. The isosurface is a specified small magnitude of an eigenvalue of the local velocity gradient tensor that indicates local swirl, and the coloration of the surface indicates the sign of the local vertical vorticity (red = positive; blue = negative). This has the shape of a hairpin vortex reaching well into the middle of the boundary layer, with a tilted orientation favorable for eddy momentum flux, $u'w' < 0$. (Sullivan *et al.*, 2016)

buoyancy oscillation time, $\tau_{igw} = N^{-1}$; this is probably why internal waves are often vigorous in this layer. Of course, once the turbulence has collapsed to a state of anisotropic stratified turbulence in the remnant layer, then the coupling with the wave field largely ceases. Another interesting scale shown in Fig. 25 is the *Thorpe scale*, L_T, defined as the r.m.s.; vertical distance parcels have to be moved in a profile $b(z)$ to achieve marginal stability, $db/dz \geq 0 \; \forall \; z$. Empirically, it is found that $L_T \approx 0.84 L_O$, indicating that overturning is actively occurring at nearly the theoretical limit predicted by the energy argument underlying the definition of L_O.

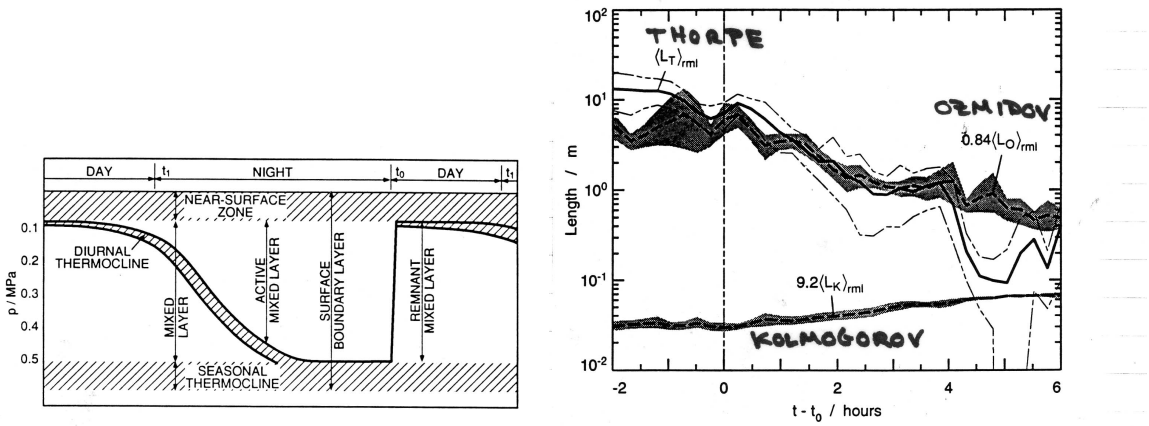

Figure 25: (Left) Regimes of the oceanic diurnal cycle. (Right) Length scales in the remnant turbulence layer: Thorpe scale L_T, Ozmidov scale L_O, and Kolmogorov scale $\eta = L_K$ that forms after $t = 0$ and then decays. (Brainerd and Gregg, 1993)

The dynamics of the SBL are best understood as a combination of Monin-Obukhov similarity near the surface and near-critical stratified shear instability, with $Ri \approx Ri_{cr} \sim 0.25$, in the outer regions (Fig. 19). For $z > h$ in the remnant layer, $Ri > Ri_{cr}$ at least intermittently. Thus, the turbulent dynamics in the outer SBL is much more local than in either the CBL or the Ekman PBL, with Kelvin-Helmholtz vortices as its dominant coherent structure. Nevertheless, we can identify a dominant length-scale,

$$h \sim \frac{u_*}{N} \,, \tag{65}$$

outside of the near-surface Monin-Obukhov and local-similarity layers (which can be very shallow in the SBL; see Fig. 1), and associate it with an interior eddy diffusivity,

$$K \sim u_* h = \frac{u_*^2}{N} \tag{66}$$

(Mahrt and Vickers, 2003). Measurements of the SBL are notoriously variable: the turbulence is relatively weak compared to other PBL regimes, and shear instability and internal waves in the overlying region often encroach down toward the surface.

4 Langmuir Boundary Layers

The upper-oceanic and lower-atmospheric PBLs can be strongly influenced by surface gravity waves on the air-sea interface. One important regime is called the *Langmuir PBL*, because Langmuir circulations are the dominant coherent structures (Figs. 26-27); it is the focus of this section. Other important surface wave effects (not further discussed here) are due to breaking waves (Sullivan *et al.*, 2007) and to wave-induced drag on the PBL winds (Sullivan *et al.*, 2008).

Figure 26: Photograph of the surface of the Great Salt Lake showing surface convergence lines due to Langmuir circulations. The wind and surface waves are into the plane of the picture. (S. Monismith, personal communication)

Surface gravity waves have phase speeds c that are given by the deep water dispersion relation,

$$c \;=\; \sqrt{g/k}\,, \tag{67}$$

where k is the horizontal wavenumber. A typical value for c is 10 ms^{-1} (for a spectrum-peak wavelength $2\pi/k$ of 60 m), which is comparable to a typical near-surface wind speed, U_a. For such waves, the slope of the sea surface ak is typically small, say 0.1 for a sea level amplitude of $a = 1$ m). Since ak is a measure of the nonlinearity of the wave dynamics, this means that they are linear to leading order. Furthermore, wave-induced particle velocities are $\mathcal{O}(akc) \approx 1$ m s^{-1}. Turbulent and mean current velocities in the oceanic PBL are typically smaller than this, comparable to $\mathcal{O}([ak]^2 c) \approx 0.1$ ms^{-1}, which as we will see is also the order of the wave-induced Lagrangian mean flow, called the Stokes drift $\mathbf{u}_h^s$. The implication of these various magnitudes is that wave-induced effects on the oceanic PBL, acting through the Stokes drift, can be as important

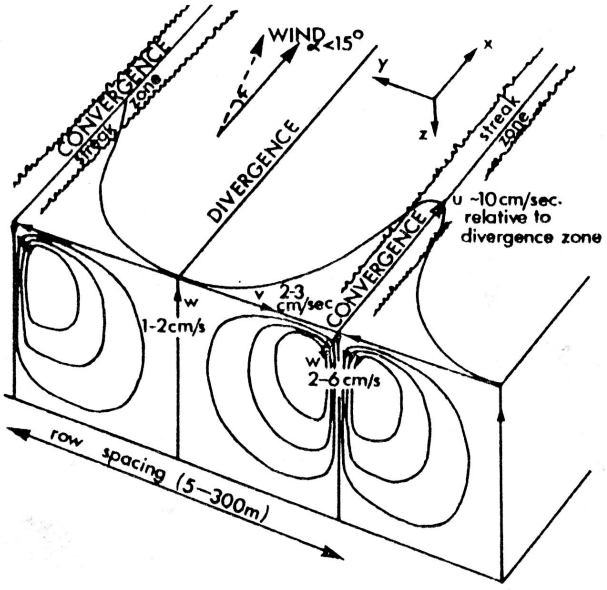

Figure 27: Sketch of the main features of Langmuir circulations. (Pollard, 1977)

as the usual turbulent nonlinear boundary-layer dynamics. In contrast, because the Stokes drift is typically much smaller than U_a, its influence on the marine atmospheric PBL is much smaller. (But there are other ways that surface waves do influence the atmospheric PBL, primarily through the "pumping" of the moving boundary.)

Surface gravity waves have a simple linear solution, assuming a small surface slope, $ak \ll 1$, deep water, $kD \ll 1$, and negligible forcing and damping:

$$\eta^w = a\cos\Phi \tag{68}$$

$$w^w = a\sigma e^{kz}\sin\Phi \tag{69}$$

$$\mathbf{u}_h^w = \hat{\mathbf{e}}_h\, a\sigma e^{kz}\cos\Phi\ , \tag{70}$$

where the mean sea level is $z = 0$, η^w is the sea level elevation of the wave, a is its amplitude, $\mathbf{k}_h$ is the horizontal wave vector, $k = |\mathbf{k}_h|$, $\hat{\mathbf{e}}_h = \mathbf{k}_h/k$, $\sigma = \sqrt{gk}$ is the frequency, and $\Phi = \mathbf{k}_h \cdot \mathbf{x}_h - \sigma t$ is the wave phase function. This solution is irrotational, with $\zeta^w = 0$. It has zero mean velocity or elevation, averaged over Φ, but it does have a mean Lagrangian motion, $\mathbf{u}^s = \hat{\mathbf{e}}_h \mathcal{U}^s(z)$. The latter arises because the wave velocity decays with depth, so the oscillatory horizontal displacements in the direction $\hat{\mathbf{e}}_h$ occur at a shallower depth than the ones in the opposite direction during the opposite phase of the oscillation, thus leading to a net displacement averaged over the cycle (Fig. 28). Mathematically, this is a solution of

$$\dot{\mathbf{x}}_h = \mathbf{u}_h(\mathbf{x}_h(t), z(t)) \tag{71}$$

$$\dot{z} = w(\mathbf{x}_h(t), z(t)). \tag{72}$$

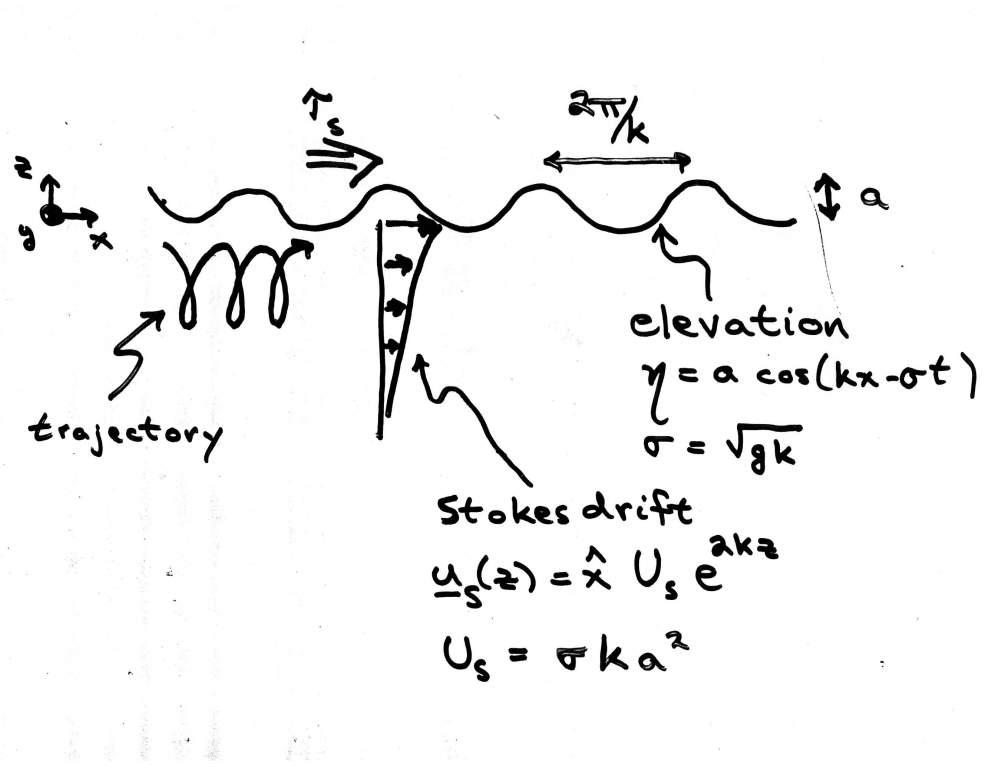

Figure 28: Sketch of surface waves and Stokes drift.

Inserting the previous solution forms, expanding in ak, and averaging over a wave phase cycle leads to

$$\mathcal{U}^s(z) \;=\; \langle [\int^t \mathbf{u}^w dt'] \cdot \nabla u^w \rangle \tag{73}$$

$$\;=\; a^2 \sigma k e^{2kz} \;, \tag{74}$$

where the angle brackets denote an average over the wave cycle, and $\mathcal{U}^s$ is the vertical profile of the Stokes velocity whose direction is equal to the surface wave propagation direction. (The derivation can be found in even ancient monographs on surface gravity waves, and in McWilliams *et al.*, 2004.)

Now consider a perturbation theory for waves and currents, where the velocity is assumed to have the form

$$\mathbf{u} \;=\; \mathbf{u}^w + (ak)^2 \left(\mathbf{v}^0 + (ak)\mathbf{v}^1 + \dots \right) \;, \tag{75}$$

where $\mathbf{v}$ has both higher order corrections to the wave dynamics, with time variability on the scale $1/\sigma$, as well as slower variability on a time scale $1/ak\sigma$ that can be calculated by averaging the dynamical equations over the wave scale. Note that $\mathbf{u}^w$ itself is $\mathcal{O}(ak)$ (consistent with a leading-order linearization) and $\mathcal{U}^s$ is $\mathcal{O}([ak]^2)$. We therefore further decompose the correction velocity fields by time scale,

$$\mathbf{v} \;=\; \langle \mathbf{v} \rangle + \mathbf{v}^w \;, \tag{76}$$

where the angle brackets denote an average over the wave and the superscript w denotes a fluctuation around the average.

We can write the vorticity equation in a uniformly rotating frame as

$$\frac{\partial \omega}{\partial t} \;=\; \nabla \times (\mathbf{u} \times [\omega + f\hat{\mathbf{z}}] - b\hat{\mathbf{z}}) + \nu \nabla^2 \omega \;. \tag{77}$$

We now insert the solution form (75)-(76) into (77), where we make a similar expansion for b and assume that f and ν are $\mathcal{O}([ak]^2)$. With reference to $\mathbf{u}^w$, (77) is trivial because the wave solution (70) is irrotational. At the leading order in ω, (77) becomes

$$\frac{\partial \omega^{0,w}}{\partial t} \;=\; 0 \;, \tag{78}$$

implying that $\omega^0 \;=\; \langle \omega^0 \rangle$. At the next order,

$$\frac{\partial \omega^{1,w}}{\partial t} \;=\; \nabla \times \left(\mathbf{u}^w \times [\langle \omega^0 \rangle + f\hat{\mathbf{z}}] \right) \;, \tag{79}$$

and, at the next,

$$\frac{\partial \langle \omega^0 \rangle}{\partial t} \;=\; \nabla \times \left(\langle \mathbf{v}^0 \rangle \times [\langle \omega^0 \rangle + f\hat{\mathbf{z}}] - \langle b^0 \rangle \hat{\mathbf{z}} \right) + \nu \nabla^2 \langle \omega^0 \rangle + \nabla \times \langle \mathbf{u}^w \times \omega^{1,w} \rangle \;. \tag{80}$$

The form of (80) is identical to that of (77), applied here to the leading order current fields, except for the addition of the final term. By manipulations of (70), (74), and (79) — as first demonstrated by Craik and Leibovich (1976) — we can derive

$$\nabla \times \langle \mathbf{u}^w \times \omega^{1,w} \rangle \;=\; \nabla \times \left(\mathbf{u}^s \times [\langle \omega^0 \rangle + f\hat{\mathbf{z}}] \right) \;, \tag{81}$$

and thus close the current dynamics at leading order. An analogous derivation can be made for the wave-averaged buoyancy equation. The upshot is that the wave-averaged Boussinesq Equations, for $(\mathbf{u}, b) \;\equiv\; (\langle \mathbf{v}^0 \rangle, \langle b^0 \rangle)$, can be written as

$$\begin{aligned} \frac{D\mathbf{u}}{Dt} &= -\nabla\phi + \nu\nabla^2\mathbf{u} + \hat{\mathbf{z}}b - f\hat{\mathbf{z}} \times (\mathbf{u} + \mathbf{u}^s) + \mathbf{u}^s \times \omega \\ \nabla \cdot \mathbf{u} &= 0 \\ \frac{Db}{Dt} &= \kappa\nabla^2 b - \mathbf{u}^s \cdot \nabla b \;. \end{aligned} \tag{82}$$

Thus, there are added advective and Coriolis *vortex forces* in the momentum balance and a *wave-added advection* in the buoyancy and other tracer balances, all of which are proportional to the Stokes drift, as well as a Bernoulli-head increment (*i.e.,* $\frac{1}{2}\mathbf{u}^{w\,2}$) that is now part of the wave-averaged pressure (McWilliams *et al.*, 2004).

Now consider a shear PBL in the presence of waves, where (82) is the governing dynamics. An obvious first problem is the analytic Ekman layer problem, where we modify (42) both for an oceanic configuration with an imposed top boundary stress τ^a and for the inclusion of the Coriolis vortex force in (82):

$$-f(V + V^s) \;=\; \nu_e \frac{\partial^2 U}{\partial z^2} \tag{83}$$

$$f(U + U^s) \;=\; \nu_e \frac{\partial^2 V}{\partial z^2} \tag{84}$$

with boundary conditions,

$$\nu_e \frac{\partial \mathbf{U}}{\partial z} \;=\; \frac{\tau^a}{\rho_0} \quad \text{at } z = 0 \tag{85}$$

$$(U, V) \;\to\; 0 \quad \text{as } z \to -\infty \,. \tag{86}$$

Here $(U^s, V^s)(z)$ are the vector components of the Stokes drift velocity $\mathbf{u}^s(z)$. If we specialize to the case where both $\mathbf{u}^s$ and τ^a are in the $\hat{\mathbf{x}}$ direction (that is appropriate for wind-generated waves), then the solution of (84)-(86) is

$$\begin{aligned} U \;&=\; \frac{\tau^a}{\rho_0 \sqrt{2 f \nu_e}}\, e^{\gamma z} \left(\cos \gamma z + \sin \gamma z\right) \;-\; D\mathcal{U}^s(z) \\ &+\; e^{\gamma z} \left(R_- \cos \gamma z \;+\; R_+ \sin \gamma z\right) \mathcal{U}^s(0) \\ V \;&=\; \frac{\tau^a}{\rho_0 \sqrt{2 f \nu_e}}\, e^{\gamma z} \left(-\cos \gamma z + \sin \gamma z\right) \;+\; 2(k/\gamma)^2 D\mathcal{U}^s(z) \\ &+\; e^{\gamma z} \left(R_- \sin \gamma z \;-\; R_+ \cos \gamma z\right) \mathcal{U}^s(0) \,, \end{aligned} \tag{87}$$

where $\gamma = \sqrt{f/2\nu_e}$ as above, $\mathcal{U}^s$ is given by (74), and

$$D = \left(1 + 4(k/\gamma)^4\right)^{-1} , \quad R_\pm = \frac{k}{\gamma} \left(1 \pm 2(k/\gamma)^2\right) D \,.$$

The hodograph for (87) is plotted in Fig. 29 for a particular set of parameters, as listed. It shows an Ekman spiral turning to the right of the surface stress for $f > 0$. However, there are now two vertical decay scales, $1/k$ and $1/\gamma$. The transport has both a component 90^o to the right of the stress, but also one opposed to the Stokes-drift transport:

$$\int_{-\infty}^{0} dz\, \mathbf{U} \;=\; -\int_{-\infty}^{0} dz\, \mathbf{U}^s \;-\; \hat{\mathbf{z}} \times \tau^a / f \,. \tag{88}$$

The wave-averaged dynamics in (82) are especially relevant to the frequently observed phenomenon of Langmuir circulations. These are longitudinal roll cells parallel to the wind and waves, made visible through the gathering of surfactants (scum) along the lines of surface convergence (Fig. 26). The essential mechanism for this can be seen in (82) by doing an early-time, rapid-distortion analysis with $f = g = 0$:

$$\omega(\mathbf{x} - \mathbf{u}^s t, t) \;=\; \omega(\mathbf{x}, 0) + \frac{d\mathbf{u}^s}{dz} \omega^{(z)}(\mathbf{x}, 0) t + \ldots \,. \tag{89}$$

The initial vorticity vector will move with the Stokes drift, and its vertical component will tilt and amplify in the longitudinal direction; thus, the vortex force is conducive to growth of the longitudinal vorticity component.

Now consider the problem of a wind-driven, upper-ocean current with Re as a control parameter, and with $f = g = 0$ for now. For small Re, the equilibrium solution is a 1D steady flow, $U(z)\hat{\mathbf{x}}$. At a critical value of Re, this flow is unstable to 2D steady rolls that are identifiable with Langmuir circulations. For larger Re, there are 3D secondary instabilities and eventually a transition to a

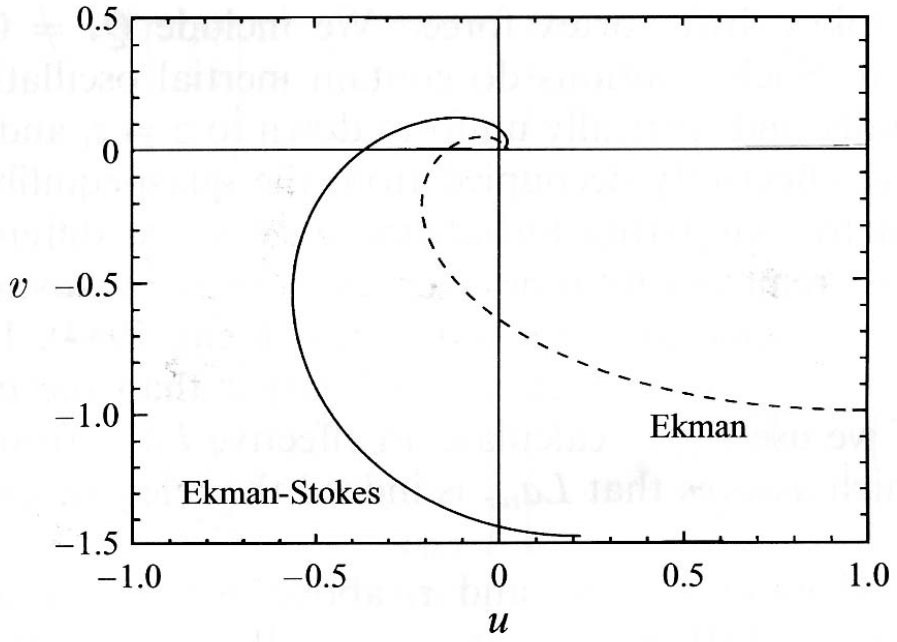

Figure 29: Hodograph of the non-dimensional laminar Stokes-Ekman layer velocity vector with $La_{tur} = 0.3$ (solid line) *vs.* the pure Ekman layer (dashed line). (McWilliams *et al.*, 1997)

fully developed flow that can be called *Langmuir turbulence*. For the ocean, we are interested in this latter stage, with a finite value of the *turbulent Langmuir number*,

$$La_{tur} \;=\; \sqrt{u_*/\mathcal{U}^s(0)}\;, \tag{90}$$

$Re \to \infty$, and $f, N \neq 0$. Empirically it has been found that $La_{tur} \approx 0.3$ in wind-wave equilibrium.

This problem has been solved with LES of the equations (82) for a horizontally homogeneous, wind-driven PBL with a weakly unstable surface buoyancy flux above a stable inversion layer (McWilliams *et al.*, 1997). The mean flow, $\overline{\mathbf{u}}_h(z)$, is in Fig. 30. It shows the effect of the Coriolis vortex force seen in the constant-ν_e solution (87)-(88), *viz.,* an enhanced turning angle to the right of the surface stress. In addition, it shows a diminished spiral, compared to the analytic solution with constant ν_e, to an even greater degree than in the turbulent Ekman solution (also shown in Fig. 30 for the identical problem configuration but for $\mathcal{U}^s = 0$ and $La_{tur} = \infty$). The TKE and ε profiles (Fig. 31) show an enhanced turbulent intensity with finite La_{tur}, and the eddy momentum flux efficiency (*i.e.,* $\nu_e(z)$ in Fig. 32) and entrainment-layer buoyancy flux (Fig. 33) are also enhanced. In particular, ε is much larger than the MO similarity prediction (16) near the surface due to wave breaking and below it decays much more steeply as $\sim z^{-2}$ due to the Langmuir turbulence enhancement of the boundary-layer energy cycle (Terray *et al.*, 1996). Thus, we conclude that the presence of the wave-added terms, and the vortex force in particular makes both the turbulence and its vertical transports stronger.

We see the turbulent Langmuir circulations in Figs. 34-36 that show surface-trapped particle trajectories and distributions and the near-surface longitudinal vorticity field. The cell structure is still evident, but it is more irregular in shape and has finite correlation scales in x and t, compared to the idealized form in Fig. 27. As a final example, Fig. 37 shows the multi-scale structure that

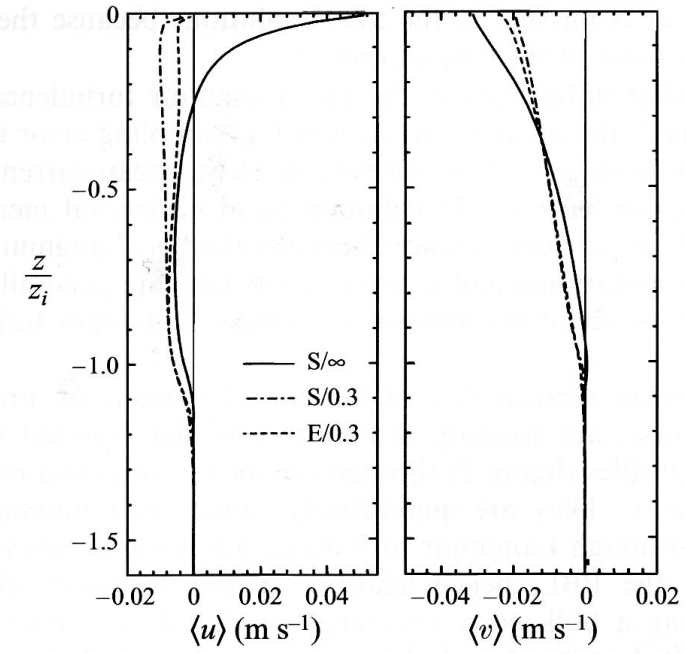

Figure 30: Horizontal and time mean velocity profiles. The solid line is for the pure Ekman layer and the broken lines are for $La_{tur} = 0.3$ in two different domain sizes. (McWilliams *et al.*, 1997)

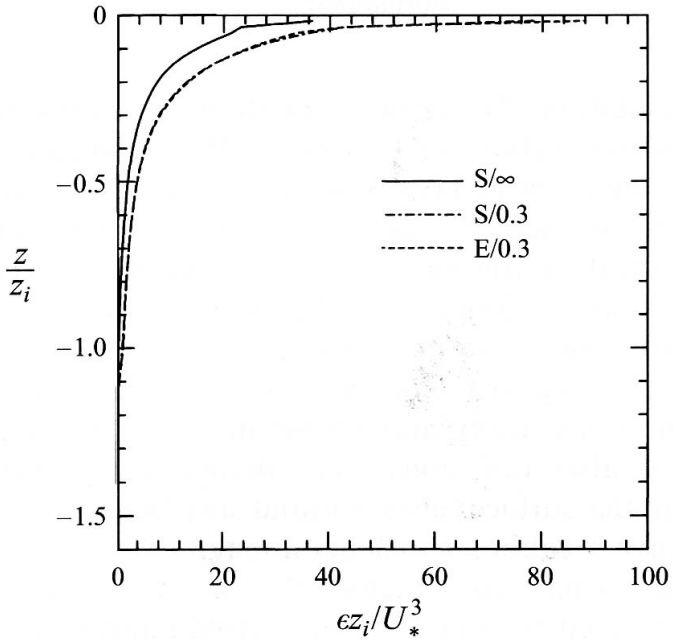

Figure 31: Mean kinetic energy dissipation rate profiles, $\varepsilon(z)$. The solid line is for the pure Ekman layer and the broken lines are for $La_{tur} = 0.3$ in two different domain sizes. (McWilliams *et al.*, 1997)

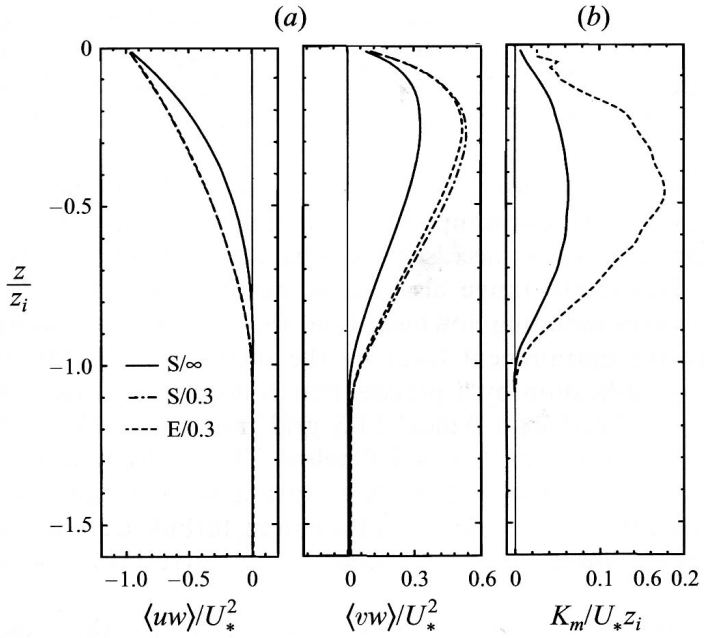

Figure 32: Mean vertical momentum flux $\overline{\mathbf{u}_h' w'}(z)$ profiles and bulk eddy viscosity $\nu_e(z)$ profiles. The solid line is for the pure Ekman layer and the broken lines are for $La_{tur} = 0.3$ in two different domain sizes. (McWilliams *et al.*, 1997)

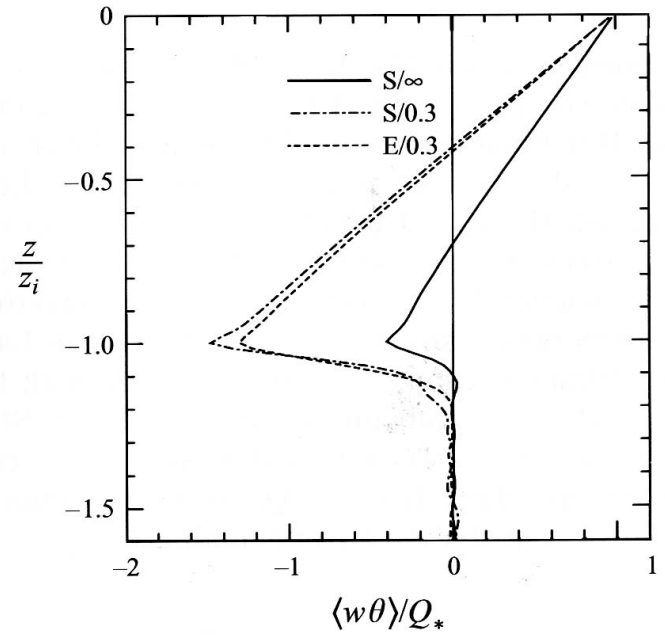

Figure 33: Mean vertical heat flux profiles normalized by the (small) surface heat flux Q_*. The solid line is for the pure Ekman layer and the broken lines are for $La_{tur} = 0.3$ in two different domain sizes. (McWilliams *et al.*, 1997)

can develop in $w(x, y)$ for Langmuir turbulence in the presence of both local-equilibrium wind waves and stronger, remotely generated swell waves.

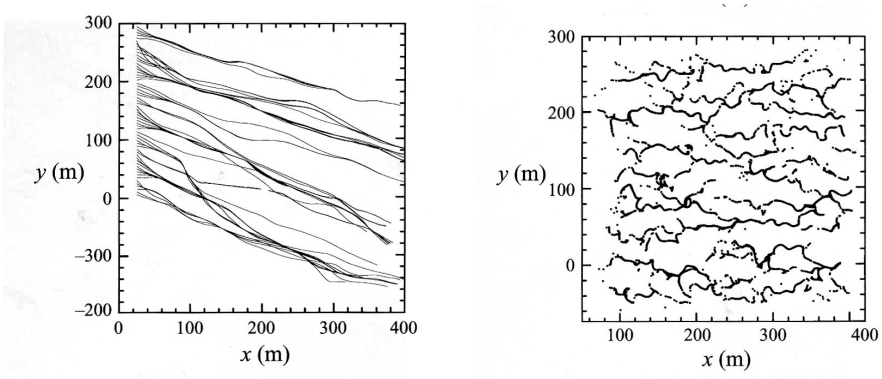

Figure 34: (a) Trajectories of surface parcels released along a transverse line over a continuous time interval in equilibrium Langmuir turbulence with $La_{tur} = 0.3$. (b) Locations of 10^4 surface parcels 1500 s after being released randomly within $0 \leq x, y \leq 300$ m. (McWilliams *et al.*, 1997)

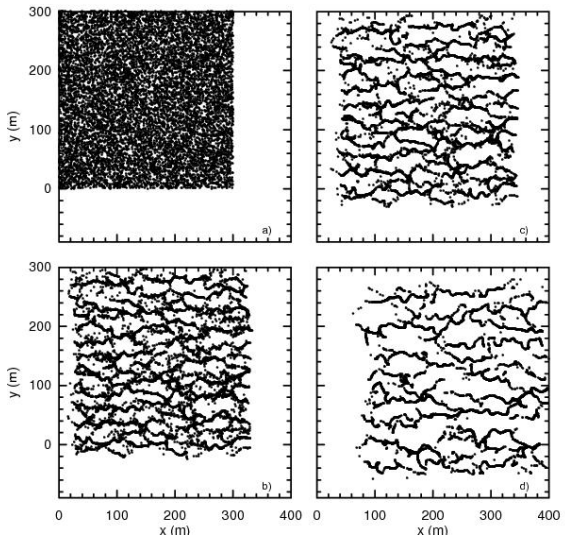

Figure 35: Distributions at successive times about 5 minutes apart for buoyant surface particles initially released randomly in the midst of oceanic equilibrium Langmuir turbulence with $La_{tur} = 0.3$. Note the gathering into surface convergence lines due to Langmuir circulations. The final panel here is the same as in Fig. 34. (McWilliams *et al.*, 1997)

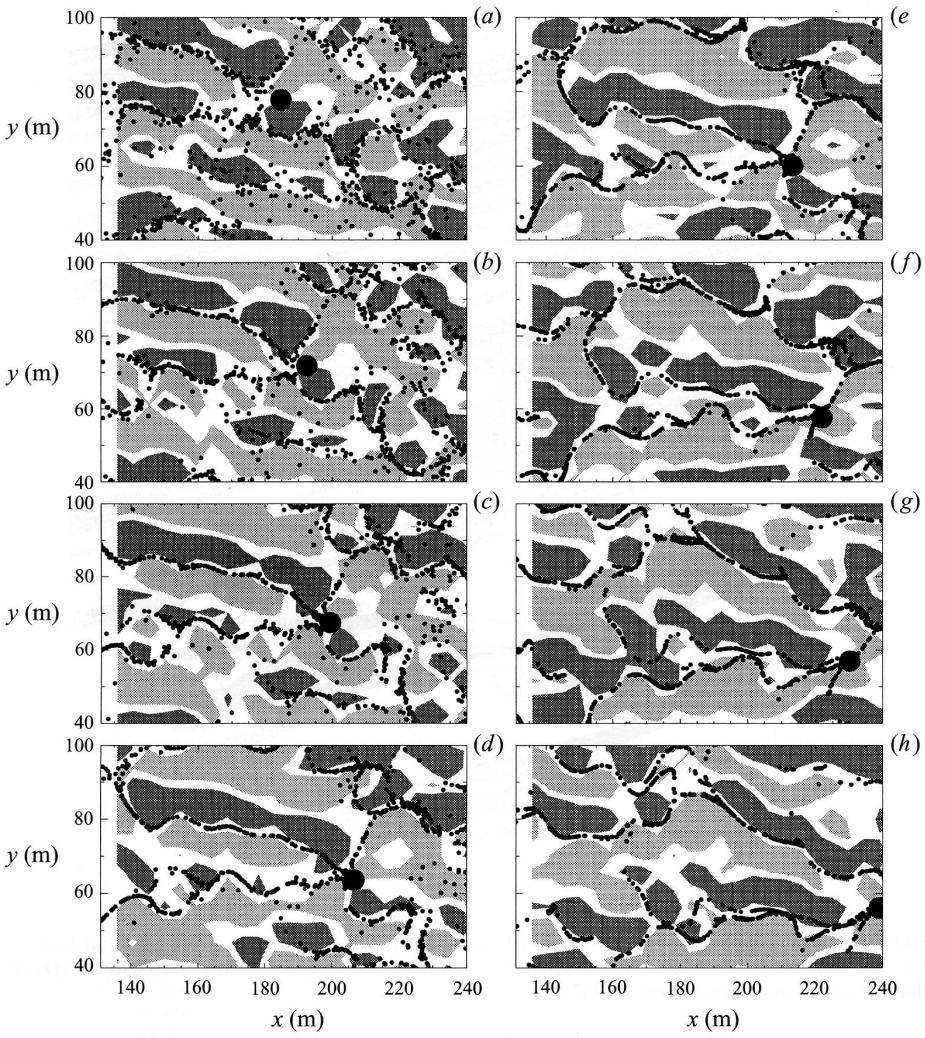

Figure 36: Temporal and spatial variation of surface particles (dots) and near-surface streamwise vorticity (light and dark shading indicate different signs above a specified threshold magnitude) in Langmuir turbulence with $La_{tur} = 0.3$. The time intervals between the panels are about 120 s. The position of a single particle that is near the early-time Y-junction of two convergence lines is indicated by the large dot. Note the merger of two circulation cells that occurs to the left of this particle. (McWilliams *et al.*, 1997)

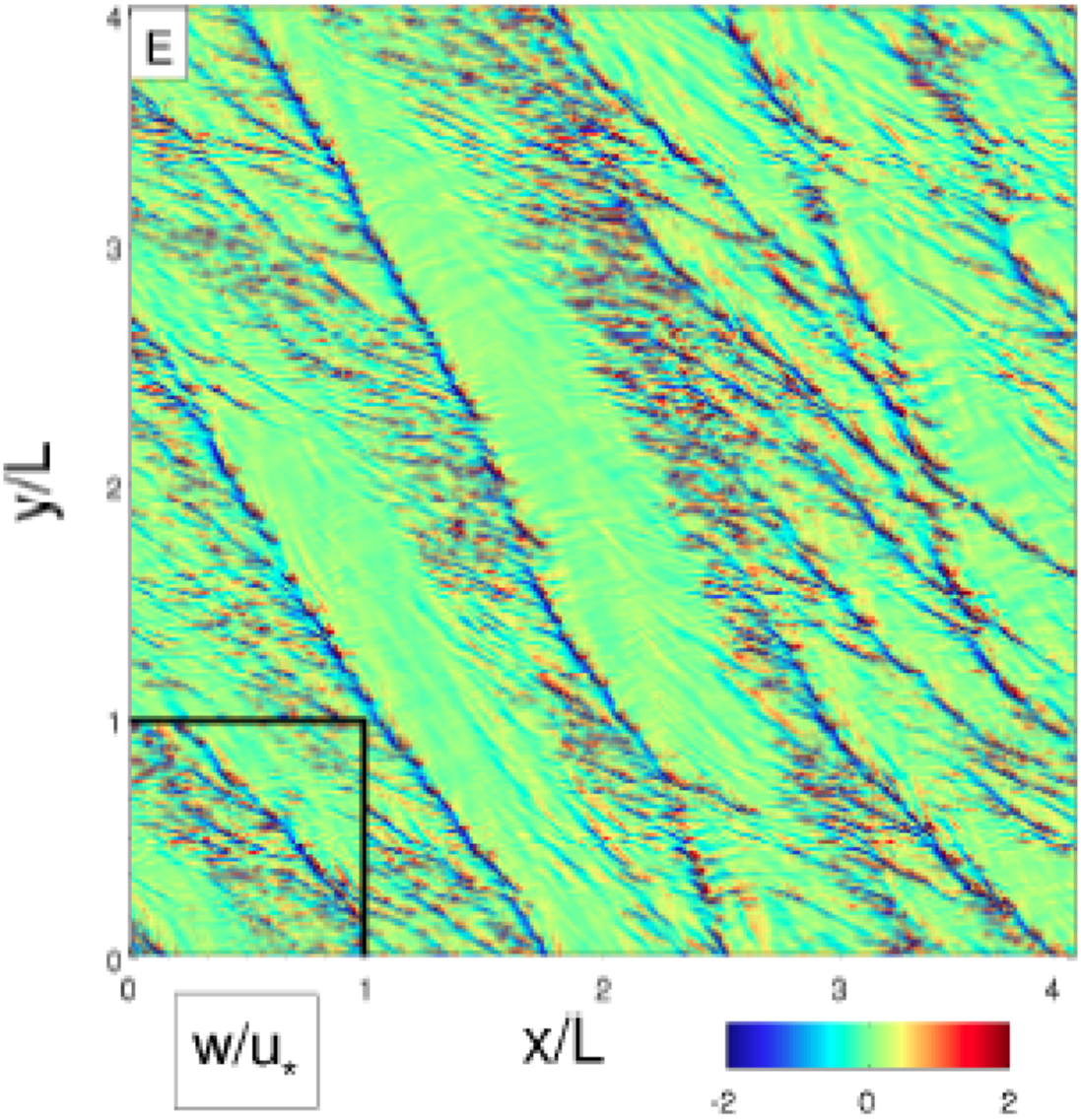

Figure 37: $w(x, y)$ snapshot at $z = -1$ m for Langmuir Turbulence with both local wind-waves and remotely generated swell waves. The horizontal width of this domain is 1200 m. (McWilliams *et al.*, 2014)

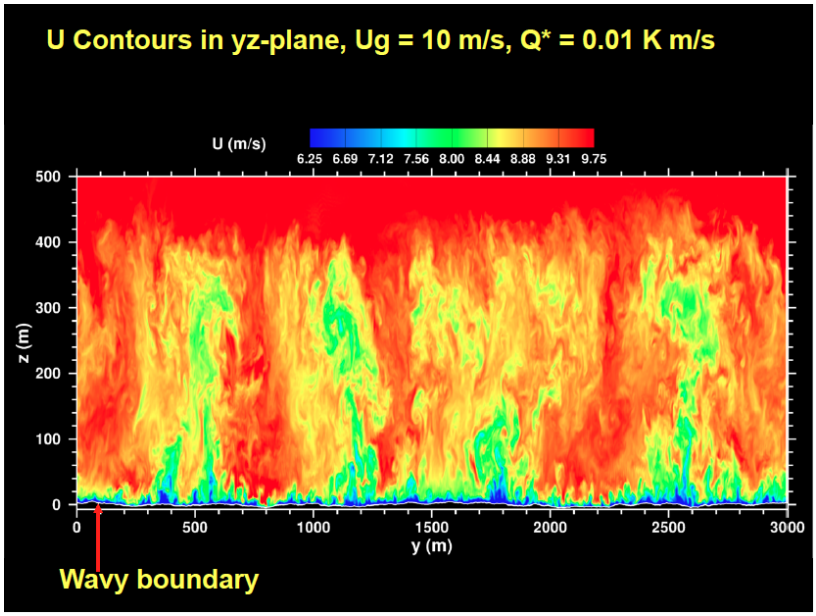

Figure 38: Wind component $u(y, z)$ in the direction of the lower-tropospheric geostrophic wind in a transverse cross-section from an atmospheric LES with a wave-specified moving lower boundary. (Sullivan *et al.*, 2014)

5 Waves Under the Atmospheric Boundary Layer

Surface waves also alter the atmospheric boundary layer compared to flow over land. Not only are waves sometimes rather large roughness elements (as are trees), but they present a moving surface as well. An important concept is that when winds drag over water, an instability of the surface interface develops and wave grow, primarily by form stress momentum transfer from winds to waves. At some point the momentum and energy input to the waves is balanced by the output to the ocean currents, mostly by wave breaking when the wind is not slow; this phase is referred to as wind-wave equilibrium. (*N.b.*, this is the true mechanism of momentum transfer from waves to currents.) A parameter that measures this progression is the wave age,

$$A = \frac{C_p}{U_a}\,, \tag{91}$$

where C_p is the phase speed of the wavenumber associated with the peak of the wave energy spectrum and U_a is a low-level wind speed (*e.g.,* at $z = 10$ m, as often used in bulk-formula estimates of surface stress). For young and growing waves, $A < 1$; for wind-wave equilibrium, $A \approx 1$; and for old waves, generated by stronger winds elsewhere or left over from previously stronger winds locally, $A > 1$. Old waves present the interesting situation where the surface is moving faster than the adjacent wind, hence the momentum flux can actually accelerate the surface wind rather than damp it.

We present several illustrations of a wavy atmospheric boundary layer simulated by LES where the water movement at the bottom is specified from measured wave spectra. Fig. 38 shows a cross-

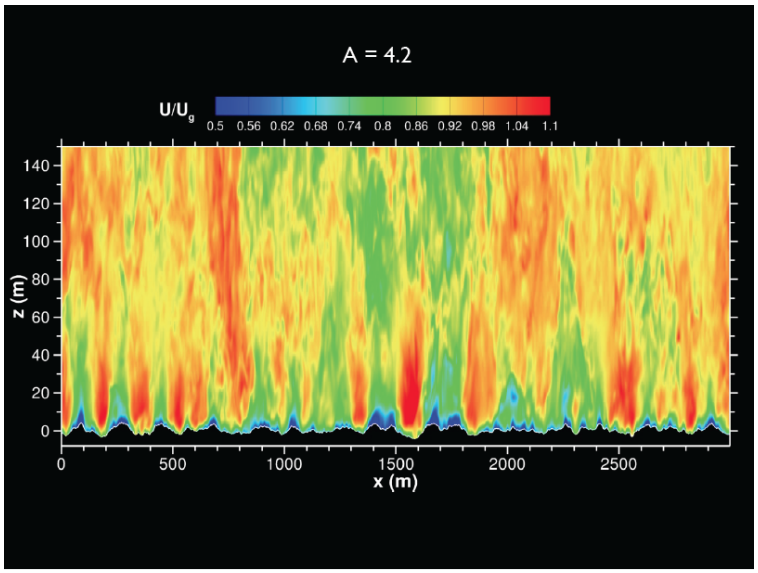

Figure 39: $u(x, z)$ in relation to surface elevation $\eta(x)$ in the lower third of the atmospheric boundary layer shown in Fig. 38. Notice the "wave-pumping" relationship between forward surface u in the troughs and backward u above the crests. The wave-pumped u signals extend only to about $z = 50$ m here (comparable to a peak wavelength). (Sullivan *et al.*, 2014)

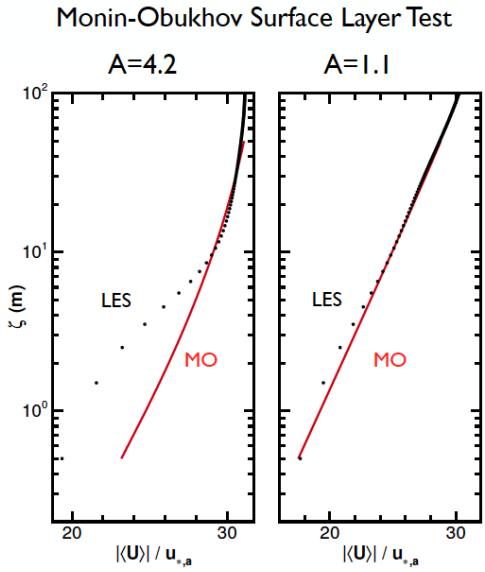

Figure 40: Profiles of the mean wind $\overline{u}(z)$ near the surface, where ζ is height above the sea surface. The surface wave pumping disrupts MO similarity over a vertical distance that is larger for larger wave age A. (Sullivan *et al.*, 2014)

section of the wind over the whole boundary layer in the direction of the atmospheric tropospheric flow at around 500 m height. The layer is primarily a shear Ekman layer with weakly convective surface flux. The large eddies are visible and here have a kind of longitudinal roll-cell pattern. Near the surface the wind is much slower, of course, but it also shows strong correlations with the local wave surface (Fig. 39 for rather old waves, $A = 4.2$); *i.e.,* the orbital motions of the waves are pushing and pumping the atmospheric eddies nearby, and in doing so these wave-pumped eddies are the ones carrying the mean momentum flux, $\overline{u'w}$, which is upward in this case. In this large-A situation the surface layer does not conform to a Monin-Obukhov similarity profile up to a height of about $z = 10$ m, although its discrepancy is limited to much lower heights $z < 1$ m with equilibrium waves (Fig. 40). In part this is because the wave-pumping effect provides another relevant length scale besides the similarity assumption of only the distance from the boundary, z.

6 K-Profile PBL Parameterization Model

Oceanic and atmospheric models of large- and meso-scale circulations need to include the effects of turbulent transport and dissipation by smaller-scale motions through parameterizations. In their fluid interiors, the usual parameterization forms are some type of eddy diffusion, though often anisotropic (*i.e.,* with $\kappa_v \ll \kappa_h$) and unequal for momentum and scalars (*i.e.,* $Pr_e \neq 1$). The effects of the PBL, however, are usually not well represented by a constant eddy diffusivity, so a number of different types of parameterization have been developed for it. Among the popular types are *mixed-layer models* (Sec. 2.1) and *local moment closure models* (*Shear Turbulence*). However, these models, respectively, can aptly be criticized because mean profiles are often not well mixed in the PBL (especially in non-convective situations) and turbulent fluxes are not entirely determined by local properties (*e.g.,* plumes in convection), especially in the entrainment layer at the interior edge of the PBL.

A different type of PBL parameterization model — called K-Profile Parameterization (KPP) — has become widely used in both atmospheric and oceanic models. KPP is still an evolving model, whose detailed rules are being changed as new observations and LES simulations are made, but its overall framework is considered to be a good match to the following criteria for utility in larger-scale models:

- It specifies the rates of turbulent mixing, not the shape of the mean profile (*cf.,* a mixed-layer model).
- It is consistent with Monin-Obukhov similarity structure near the surface (Sec. 1.1).
- It is intended to span a wide range of regimes in surface fluxes and mean profiles.
- It has vertically nonlocal transport (especially in convection).
- It has continuity with interior mixing processes.
- It is computationally compatible with a GCM (*i.e.,* it can be calculated on a discrete grid and is not too expensive).

On the other hand, it is reasonable to have somewhat limited expectations for a useful parameterization, whether KPP or some other type: it must represent the hypothesized essential effects with qualitative validity; it must be fit and assessed quantitatively in at least some situations; and it must not lead to silly answers in general applications, even though it might not always be particularly accurate.

In KPP the evolution of a fluid quantity Q (*i.e.,* horizontal velocity or a material tracer) is influenced by transport and mixing according to an equation of the following form:

$$\frac{\partial \langle Q \rangle}{\partial t} \;=\; \ldots \;-\; \frac{\partial F_Q}{\partial z}\,, \tag{92}$$

where the angle brackets denote an average in time and horizontal position over the scales of boundary-layer turbulence; F_Q is the mean vertical flux of Q by the waves, turbulence, and molecular diffusion,

$$F_Q(z) \;\equiv\; \langle Q'w' \rangle \;-\; \kappa_m \frac{\partial \langle Q \rangle}{\partial z} \tag{93}$$

(κ_m is the molecular diffusivity); and the dots denote other evolutionary influences unrelated to the turbulence, including any non-conservative material processes or even buoyancy forces (as for aerosols in air and bubbles and oil droplets in water). In the KPP model the flux within the boundary layer, $0 \geq z \geq -h$ (*i.e.,* for definiteness, we will work within an oceanic surface-layer geometry), has the following form:

$$F_Q(z) \;=\; -\,\kappa_v(z) \left[\frac{\partial \langle Q \rangle}{\partial z} \;-\; \gamma_Q \right], \tag{94}$$

where κ_v is a positive eddy diffusivity, γ — called the counter-gradient flux by Deardorff (1972) — appears here as an augmentation of the mean Q gradient, and $-\kappa_v \gamma$ is a flux profile independent of the mean gradient. O'Brien (1970) noted that κ_v usually has a convex structure in the boundary layer. With this assumption as its basis plus a rule to determine the PBL thickness h, KPP was formulated and tested empirically as an atmospheric model in Troen and Mahrt (1986) and as an oceanic model in Large *et al.* (1994). KPP is a non-local, mean-field closure model, since κ and γ are functionals of the surface boundary fluxes and mean quantities throughout the whole boundary layer.

Now we describe the rules for KPP for an oceanic surface PBL, $-\,h \leq z \leq 0$; similar rules apply to atmospheric and oceanic bottom PBLs. The eddy diffusivity, $\kappa(z)$, is assumed to have a self-similar, convex shape across the boundary layer and an amplitude related to the fluxes at the edges of the layer. Its formula is

$$\kappa_v(z) \;=\; W h\, G(\sigma)\,, \tag{95}$$

where $\sigma \;=\; -z/h$ is the normalized depth within the layer. $G(\sigma)$ is the shape function. In the canonical situation with M-O similarity structure near $z = 0$ and negligible mixing below $z = -h$, then

$$G \;=\; \sigma(1-\sigma)^2\,, \tag{96}$$

which vanishes at the top and bottom of the boundary layer (*i.e.,* $\sigma \;= 0$ and -1, respectively) and has a maximum value of 0.15 at $\sigma \;=\; 0.33$. W is a turbulent velocity scale,

$$W \;=\; \frac{k\, u_*}{\Phi}\,, \tag{97}$$

where k (= 0.4) is von Karman's constant and Φ is the stability function in M-O theory (Sec. 1.1. In the KPP model ϕ is a function of h/L outside of the near-surface layer (*i.e.,* $0 \geq -z \geq 0.1h$), and its values differ between scalar quantities and momentum when $L < 0$). L is the Monin-Obukhov length defined in (2). The non-gradient flux, $\gamma(z)$, is assumed in KPP to have a uniform profile throughout the interior part of the boundary layer,

$$\gamma \;=\; C_\gamma \frac{F_Q(0)}{W\, h}\,, \tag{98}$$

where C_γ is a positive constant. This formula implies that, after the multiplication by the positive, convex $\kappa_v(z)$ in (94), there is a transport of Q from the upper part of the boundary layer (*i.e.,* above the maximum in G) to the lower part (below the maximum) in the sense set by the sign of the surface flux, $F_Q(0)$. For example, surface cooling implies $F_T(0) > 0$, hence $\gamma > 0$, hence $-\kappa\gamma < 0$ and its divergence acts in (27) to increase T in the upper part of the boundary layer and cool the lower part and thus contributes to the movement of heat from below up towards the surface. Thus, (98) represents an intrinsically non-local flux process, since it is not linked to the local mean gradient at any particular depth. The utility of γ was recognized by Deardorff (1972) for convective boundary layers in which gravitationally unstable plumes carry heat and material across the boundary layer, even though the interior mean gradients are small; of course, an analogous statement can be made for the Langmuir Cells, some of which also span the whole boundary layer (McWilliams and Sullivan, 2001). For temperature in thermal convection, the mean gradient even reverses sign within the layer, due to entrainment of interior fluid that provides a heat flux near the edge of the layer with a sign opposite to the surface flux, but the sign reversals of F_Q and $\partial\langle Q\rangle/\partial z$ rarely occur at the same z value. Thus, γ can prevent singularities and negative values in $\kappa(z)$ when (94) is fit to actual profiles of $F_Q(z)$ and $\langle Q\rangle(z)$, and γ is commonly fit simultaneously to make $\kappa(z) > 0$ and smooth in z. Without γ, an eddy-diffusion model like (92)-(94), with a smooth, positive κ, will make $\langle Q\rangle(z,t)$ evolve such that zeros in F_Q and the mean gradient occur in the same location, unlike what is observed in convective boundary layers, for example.

The boundary-layer depth, h, is determined in KPP as the first non-zero depth, $z \leq 0$, at which $Cr(z) = 0$, where

$$\begin{aligned} Cr(z) \;&=\; \int_z^0 J(z') \left[\left(\frac{\partial \mathbf{u}}{\partial z} \right)^2 - \frac{N^2(z)}{Ri_c} - C_{ek} f^2 \right] dz' \;+\; \frac{V_t^2(z)}{|z|} \\ &\equiv \qquad\quad \mathcal{I}_{sh} \quad - \quad \mathcal{I}_{st} \quad - \quad \mathcal{I}_{rot} \quad + \quad \mathcal{I}_{ent}\,. \end{aligned} \tag{99}$$

$N^2 = \alpha g \partial T/\partial z$ is the square of the Brunt-Vaisalla frequency. $J(z) = |z|/(|z| + \epsilon h)$ is a weighting function that excludes the surface Monin-Obukhov layer from controlling the extent of the boundary layer; *i.e.,* $0 > z \geq -\epsilon h$, assuming $\epsilon \ll 1$ ($\epsilon = 0.1$ here). The component $\mathcal{I}(z)$ terms in $Cr(z)$ are, respectively, the destabilizing mean shear, the (usually) stabilizing stratification, the stabilizing rotation, and the destabilizing turbulent entrainment at the interior interface. The turbulent entrainment term has a velocity magnitude $V_t = C_{ent}[\, w_s(z) N(z) |z|\,]^{1/2}$, where $w_s(z)$ is the usual turbulent velocity magnitude in KPP. The constants $C_{ek} = 211$, $Ri_c = 0.3$, and $C_{ent} = 5.07$ are determined by fitting KPP solutions to extreme situations where the empirical results are well known. These are, respectively, the situations of non-rotating, penetrative free convection ($\mathcal{I}_{st} = \mathcal{I}_{ent}$), an unstratified Ekman layer ($\mathcal{I}_{sh} = \mathcal{I}_{rot}$), and a stratified shear layer ($\mathcal{I}_{st} = \mathcal{I}_{sh}$). In more general

circumstances the $Cr(-h) = 0$ condition allows for smooth transitions among these different stabilizing and destabilizing influences, without requiring any logical if-tests in the code. The original KPP rules for h are differently expressed but give rather similar answers to (99).

Examples of KPP solutions are in Large and Crawford (1995), McWilliams and Huckle (2006), and McWilliams *et al.* (2009). A future development is to include surface gravity wave effects (Secs. 4-5).

References

Brainerd, K.E., and M.C. Gregg, 1993: Diurnal restratification and turbulence in the oceanic surface mixed layer 1. Observations. *J. Geophys. Res.* **98**, 22645-22656.

Brainerd, K.E., and M.C. Gregg, 1995: Surface mixed and mixing layer depths, *Deep Sea Res.* **42**, 1521-1543.

Businger, J.A., 1970: Turbulent transfer in the atmospheric surface layer. *Workshop on Micrometeorology*, American Meteorol. Soc., 67-100.

Caughey, S.J., J.C. Wyngaard, and J.C. Kaimal, 1979: turbulence in the evolving stable boundary layer. *J. Atmos. Sci.* **36**, 1041-1052.

Coleman, G.N, 1999: Similarity statistics from a direct numerical simulation of the neutrally stratified planetary boundary layer. *J. Atmos. Sci.* **56**, 891-900.

Craik, A.D.D., and S. Leibovich, S., 1976: A rational model for Langmuir circulations. *J. Fluid Mech.* **73**, 401-426.

Deardorff, J., 1970: Convective velocity and temperature scales for the unstable planetary boundary layer and for Rayleigh convection. *J. Atmos. Sci.* **27**, 1211-1213.

Deardorff, J., 1972: Theoretical expression for the counter-gradient vertical heat flux. *J. Geophys. Res.* **77**, 5900-5904.

Kaimal, J.C., J.C. Wyngaard, D.A. Haugen, O.R. Cote, Y. Izumi, S.J. Caughey and C.J. Readings, 1976: Turbulence Structure in the convective boundary layer. *J. Atmos. Sci.* **33**, 2152-2169.

Large, W.G., J.C. McWilliams, and S.C. Doney, 1994: Oceanic vertical mixing: a review and a model with a non-local K-profile boundary layer parameterization. *Rev. Geophys.* **32**, 363-403.

Large, W.G., and G.B. Crawford, 1995: Observations and simulations of upper-ocean response to wind events during the Ocean Storms Experiment. *J. Phys. Ocean.* **25**, 2831-2582.

Lenschow, D.H., J.C. Wyngaard, W.T. Pennell, 1980: Mean-field and second-moment budgets in a baroclinic, convective boundary layer, *J. Atmos. Sci.* **37**, 1313-1326.

Lilly, D., 1968: Models of cloud-topped mixed layers under a strong inversion. *Quart. J. Royal Meteorol. Soc.* **94**, 292-309.

Mahrt, L., 1999: Stratified atmospheric boundary layers, *Boundar. Layer. Meteor.* **90**, 375-396.

Mahrt, L., and D. Vickers, 2003: Formulation of turbulent fluxes in the stable boundary layer. *J. Atmos. Sci.* **60**, 2538-2548.

McWilliams, J.C., P.P Sullivan, and C.H. Moeng, 1997: Langmuir turbulence in the ocean. *J. Fluid Mech.* **334**, 1-30.

McWilliams, J.C., and P.P. Sullivan, 2001: Vertical mixing by Langmuir circulations. *Spill Science and Technology* **6**, 225-237.

McWilliams, J.C., J.M. Restrepo, & E.M. Lane, 2004: An asymptotic theory for the interaction of waves and currents in coastal waters. *J. Fluid Mech.* **511**, 135-178.

McWilliams, J.C., and E. Huckle, 2006: Ekman layer rectification, *J. Phys. Ocean.* **36**, 1646-1659.

McWilliams, J.C., E. Huckle, and A. Shcheptkin, 2009: Buoyancy effects in a stratified Ekman layer. *J. Phys. Ocean.* **39**, 2581-2599.

McWilliams, J.C., E. Huckle, J. Liang, & P. Sullivan, 2014: Langmuir Turbulence in swell. *J. Phys. Ocean.* **44**, 870-890.

Moeng, C.H., and J.C. Wyngaard, 1989: Evaluation of turbulent transport and dissipation closures in second-order modeling, *J. Atmos. Sci.* **46**, 2311-2330.

Nieuwstadt, F.T.M., 1984: The turbulent structure of the stable, nocturnal boundary layer. *J. Atmos. Sci.* **41**, 2202-2216.

O'Brien, J.J., 1970: A note on the vertical structure of the eddy exchange coefficient in the planetary boundary layer. *J. Atmos. Sci.* **27**, 1213-1215.

Pollard, R.T., 1977: Observations and theories of Langmuir circulations and their role in near surface mixing. *A Voyage of Discovery: George Deacon's 70th Anniversary Volume*, M. Angel (ed.), Pergamon Press, 235-251.

Sorbjan, Z. 1989: *Structure of the Atmospheric Boundary Layer*, Prentice Hall.

Stevens *et al.*, 2001: Simulations of trade-wind cumuli under a strong inversion *J. Atmos. Sci.* **58**, 1870-1891.

Stevens, B., 2005: Atmospheric moist convection. *Ann. Rev. Earth & Planetary Sci.* **33**, 605-643.

Stevens *et al.*, 2005: Evaluation of large-eddy simulations via observations of nocturnal marine stratocumulus. *Mon. Weather Review* **133**, 1443-1462.

Sullivan, P.P., C.H. Moeng, B. Stevens, D.H. Lenschow, and S.D. Mayor, 1998: Entrainment and structure of the inversion layer in the convective planetary boundary layer. *J. Atrmos. Sci.* **55**, 3042-3064.

Sullivan, P.P., J.C. McWilliams, and W.K. Melville, 2007: Surface gravity wave effects in the oceanic boundary layer: Large Eddy Simulation with vortex force and stochastic breakers. *J. Fluid Mech.* **593**, 405-452.

Sullivan, P.P, J.B. Edson, T. Hristov, and J.C. McWilliams, 2008: Large eddy simulations and observations of atmospheric marine boundary layers above non-equilibrium surface waves. *J. Atmos. Sci.* **65**, 1225-1245.

Sullivan, P.P., J.C. McWilliams, & E.G. Patton, 2014: Large eddy simulation model of marine atmospheric boundary layers above a spectrum of moving waves. *J. Atmos. Sci.* **71**, 4001-4027.

Sullivan, P.P., J.C. Weil, E.G. Patton, H.J.J. Jonker, and D.V. Mironov, 2016: Turbulent winds and temperature fronts in large-eddy simulations of the stable atmospheric boundary layer. *J. Atmos. Sci.* **73**, 1815-1840.

Terray, E., M. Donelan, Y. Agrawal, W. Drennan, K. Kahma, A. Williams, P. Hwang, and S. Kitaigorodskii, 1996: Estimates of kinetic energy dissipation under breaking waves. *J. Phys. Ocean* **26**, 792807.

Troen, I.B., and L. Mahrt, 1986: A simple model of the atmospheric boundary layer: Sensitivity to surface evaporation. *Boundary Layer Met.* **37**, 129-148.

Wyngaard, J.C., O.R. Cote and Y. Izumi, 1971: Local free convection, similarity, and the budgets of shear stress and heat flux, *J. Atmos. Sci.* **28**, 1171-1182.

Wyngaard, J.C., 1975: Modeling the planetary boundary layer: Extension to the stable case. *Boundary-Layer Met.* **9**, 441-460.

Wyngaard, J.C., and R.A. Brost, 1984: Top-down and bottom-up diffusion of a scalar in the convective boundary layer. *J. Atmos. Sci.* **41**, 102-112.